Large-eddy simulations coupled to a spectral wave model for enhanced metocean modelling in offshore wind farms

J.G.F. van Eck

TUDelft
Delft
University of
Technology

Large-eddy simulations coupled to a spectral wave model for enhanced metocean modelling in offshore wind farms

by

J.G.F. van Eck

in partial fulfillment of the requirements for the degree of

Master of Science
in Applied Physics

at the Delft University of Technology

October 16, 2019

Supervisors:	Prof. dr. H.J.J. Jonker,	TU Delft, Whiffle
	Dr. Ir. R.A. Verzijlbergh,	TU Delft, Whiffle
	Drs. E. Wiegant,	Whiffle
	Ir. M.B. van der Meulen,	Siemens Gamesa
Committee:	Prof. dr. H.J.J. Jonker,	TU Delft, Whiffle
	Dr. S.R. de Roode,	TU Delft
	Dr. S. Kenjereš,	TU Delft

Cover photo: Gemini Wind Park

Abstract

Offshore wind energy is considered as a powerful form of renewable energy generation. It plays an important role in accelerating the world's transition towards sustainable energy sources and reducing carbon emissions by fossil fuels. This study focuses on the advancement of service planning, related to this renewable energy source, by researching high resolution metocean modelling. The research aims to assess and advance the modelling performance of typical metocean parameters by using atmospheric large-eddy simulations coupled to a spectral wave model. The GPU-Resident Atmospheric Simulation Platform (GRASP) coupled to Simulating WAves Nearshore (SWAN) was used to simulate the atmospheric- and oceanic conditions in the Gemini wind farm, located in Dutch waters. Large-scale boundary- and initial conditions were provided by the fifth generation of ECMWF's ReAnalysis (ERA5).

Relevant metocean parameters were modelled using two different coupling configurations. The one-way coupled simulation concerns the forcing of SWAN by GRASP friction velocities, for an accurate representation of the one-way momentum exchange to the ocean surface. The two-way coupled simulation concerns the momentum exchange of the friction velocity and roughness length. To accurately represent the sea surface roughness, the parameterization of Taylor and Yelland (2001) was used in this study. Both coupled configurations were used to simulate the first two months of 2017, which were subsequently validated using the available observations.

This study revealed that both coupled simulations caused a reduced value for the roughness length in wind- and wave wake conditions. Furthermore, a spatially averaged reduction in the sea state is observed due to the wake effect, where the magnitude of this wave deficit follows the line of a typical wind turbine thrust curve. The effect is however small compared to a realistic significant wave height. Besides, the two-way coupled simulations provided higher average roughness lengths in comparison to the one-way coupled simulations. This resulted in higher friction velocities and drag coefficients for the two-way coupled simulations, which subsequently reduced the time- and slab averaged wind profiles.

Moreover, the modelling performance of SWAN improves when it is forced by GRASP friction velocities instead of ERA5 wind fields. In addition, the established two-way coupled simulation is proven to be enhancement for the spectral wave model in comparison to the one-way coupled configuration. The performance of the atmospheric large-eddy simulation could also benefit from the two-way coupled configuration. However, it is sensitive to the implemented roughness length parameterization.

Acknowledgements

Table of Contents

List of Figures

List of Tables

Nomenclature

List of Acronyms

ASPIRE	Atmospheric Simulation Platform for Innovation Research Education
CPU	Central Processing Unit
DALES	Dutch Atmospheric Large-Eddy Simulation
DTM	Digital Terrain Model
ECMWF	European Centre for Mid-Range Weather Forecasts
ERA5	ECMWF ReAnalysis 5
GALES	GPU-resident Atmospheric Large-Eddy Simulation
GCM	General Circulation Model
GPU	Graphical Processing Unit
GRASP	GPU-Resident Atmospheric Simulation Platform
IFS	Integrated Forecasting System
JONSWAP	JOint North Sea WAve Project
KNMI	Royal Dutch Meteorological Institute
LAM	Limited Area Model
LES	Large-Eddy Simulation
LHVS	Land High Voltage Station
NWP	Numerical Weather Prediction
OHVS	Offshore High Voltage Station
OWF	Offshore Wind Farms

SGRE	Siemens Gamesa Renewable Energy
SOV	Service Operation Vessel
SWAN	Simulating WAves Nearshore
TUD	TU Delft
WAM	Wave Modelling Group
WRF	Weather Research and Forecasting model
WUR	Wageningen University and Research

List of Symbols

α	Phase of wave
β	Empirical parameter
χ_i^0	Prognostic variable in the precursor
χ_i^1	Prognostic variable in the cursor
η	Nudge factor
Γ	Gamma function
γ	Empirical parameter
κ	Von Kármán constant
ω	Angular frequency
ϕ_m	Stability function of momentum
π	Modified pressure
Ψ_H	Integrated stability function for heat
Ψ_M	Integrated stability function for momentum
ρ	Density
ρ_a	Density of air
ρ_w	Density of water
σ_θ	Directional width
τ_{ij}	Subgrid momentum flux
θ	Potential temperature
θ_l	Liquid water potential temperature
θ_v	Virtual potential temperature
θ_{wave}	Wave direction
θ_{wind}	Wind direction
ξ	Defined variable
ζ	Dimensionless stability parameter
$\widetilde{u}_i$	Resolved velocity component

c_θ	Refraction- or diffraction-induced turning rate
$c_{g,x}$	Group velocity in the x direction
$c_{g,y}$	Group velocity in the y-direction
c_{pd}	Specific heat capacity of dry air
c_p	Specific heat capacity
C_T'	Disk-based thrust coefficient
D	Rotor diameter
$D(f,\theta)$	Directional distribution
$E(f,\theta)$	Wave energy spectrum
f	Frequency
H_s	Significant wave height
K	Diffusivity coefficient
k	Wave number
L	Obukhov length
L_{heat}	Latent heat
L_{wave}	Wave length
m	Power of directional spreading
N	Number of frequencies
p	Pressure
p_0	Reference pressure
q_c	Cloud specific humidity
q_i	Ice specific humidity
q_l	Liquid water specific humidity
q_r	Precipitating water specific humidity
q_t	Total specific humidity
q_v	Water vapor specific humidity
R	Gas constant
r	Mixing ratio
R_d	Gas constant of dry air
$R_{u_j,\phi}$	Subgrid scalar flux
S_ϕ	Source term
S_{bfr}	Bottom friction
S_{diss}	Dissipation
S_{in}	Wave generation by wind
S_{nl3}	Triad wave-wave interaction
S_{nl4}	Quadruplet wave-wave interaction
S_{surf}	Surf-breaking
S_{wc}	White-capping
T	Absolute temperature
T_{m-10}	Mean absolute period

T_p	Peak wave period
u_*	Friction velocity
U_{10}	Wind speed at 10 meter height
U_d	Time-averaged disk-average axial velocity
u_i	Velocity component
u_i'	Subgrid velocity component
w	Wave spectral directional width
z	Vertical length scale
z_{0h}	Roughness length for heat
z_0	Roughness length

Chapter 1

Introduction

1-1 Background

On the 12$^{\text{th}}$ of December 2015 a new climate agreement was signed by 195 countries. The goal is to reduce global carbon dioxide emissions by 80 to 95 percent in 2050 for industrialized countries in comparison to 1990. Especially for the Netherlands this is going to be a big challenge. Mainly because by the end of 2018 the total percentage of energy produced by renewable sources accounted only for 7.3% of the total amount, this has to be increased to 14% in 2020 and up to 16% in 2023 according to the Dutch Energy Agreement (EZK, 2016). Furthermore, the concept of the Dutch Climate Agreement prescribes a total carbon dioxide reduction of 49% already in 2030 (EZK, 2019). Therefore, our total energy system needs to be transformed, where energy is mainly generated by renewable energy sources.

The Netherlands is currently massively expanding its offshore wind farm capacity to meet their agreed targets. The government is doing this by setting up tenders for offshore wind farm lots, which resulted in the first subsidy free tender in 2018. This is very encouraging for the cost reductions of offshore wind farms. However, in order to continue this line of cost reductions, offshore wind farms need to become even more efficient. Operation & maintenance (O&M) activities in offshore wind farms, as stated by Röckmann et al. (2017), represent a big part of the total costs of these projects, typically 25-30% of the total life cycle costs for offshore wind farms. Therefore, it is important to further reduce these costs. The most important area of cost reduction in O&M could be maintenance on offshore wind turbines because nowadays, service vessels are used inefficiently. The main reason of this lack of efficiency has to do with the fact that service vessels can only operate under certain restrictions regarding sea states and atmospheric conditions which make these vessels highly dependent on local weather forecasts for their operations. Nowadays, weather forecasts prove rather unreliable and mainly provide a coarse resolution. Therefore, it is essential to improve the performance of these weather forecasts, to obtain highly reliable local atmospheric- and ocean forecasts (metocean forecasts) at offshore wind farms (OWF). Especially wind- and wave height forecasts are of main concern.

1-2   Weather forecasting for offshore wind farms

In order to make the transition towards sustainable energy successful, not only costs reductions are important. The increase in predictability of these sustainable energy assets is also important in order to compete with conventional power plants, which have the ability to adjust their power output when necessary. For example, solar energy generation is dependent on the amount of incoming radiation on the Earth's surface. Therefore, accurate solar radiation forecast (i.e. cloud forecast) are necessary in order to accurately forecast the power output of solar energy. The same is necessary for (offshore) wind farms, their predictability performance is twofold:

- Performance of power forecast

- Performance of metocean forecast

In the first place, a reliable prediction of the power output is of importance because of the trading of electricity. The electricity produced tomorrow is traded today, called the day-ahead market. At this market, an electricity producer (utility) indicates how much electricity it is going to produce tomorrow and at which price. If it turns out that the producer cannot deliver on its production targets, it needs to pay imbalance costs to the grid operator. Therefore, an increase in weather prediction performance immediately impacts imbalance costs.

In the second place, a reliable weather forecast is important for service vessels operating in an offshore wind farm. Now not only atmospheric conditions are important, also reliable information about the local sea state is important for the operating service vessels, which can only operate under certain metocean restrictions. If more accurate and reliable local weather forecasts are provided, it will directly lead to more reliable weather windows, which are necessary in order to plan maintenance activities on wind turbines the day before. Inaccurate weather forecast can therefore result in inefficient use of service vessels and personnel. Besides weather forecasting, also weather hindcasting is important for metocean site assessments and offshore wind farm design.

The wind energy sector often uses large scale weather models, called General Circulation Models (GCMs), to obtain their weather forecast and hindcast. A statistical post processing of the obtained GCM data is often used to further strengthen the forecast. However, the weather prediction performance of these GCM varies significantly and it also lacks the resolution to account for local processes like turbulence, cloud forming, wake-effects of wind turbines and its impact on the local sea state. However, GCMs also provide weather forecasts in the form of wave forecasts. The relevant GCM has a fully integrated wave model, because wave generation is highly dependent on wind near the ocean surface. Although waves are less dependent on local processes as the atmosphere, local variations in the wind profile could have an impact on the wave modelling results. Furthermore, waves also have an impact on the atmosphere in the form of their influence on the roughness length, which is essentially the lower boundary condition of the atmospheric model. In most atmospheric models, this roughness length is considered as a constant over the entire domain. In more advanced (high resolution) atmospheric models, the roughness length is approximated with the help of a time- and space dependent relation. However, this relation lacks the dependency on the time- and space varying sea state at offshore sites. Implementation of such a dependency on the sea state should be beneficial for high resolution atmospheric models. Subsequently, a high resolution wind field could have an impact on the local sea state.

1-3   Finecasting in offshore wind farms

Over the last years, the development of nesting large-eddy simulation (LES) in a GCM proved to be a breakthrough in high resolution numerical weather prediction (NWP) (Moeng and Sullivan, 2002). Since LES became computationally feasible when a LES code was ported to graphical processes units (GPU) (Schalkwijk, 2015), it also had the potential to become an operational weather modelling technique. Furthermore, it made LES suitable to use as a wind power forecast model (van Dorp, 2016). In a LES based forecast model, the wind power is calculated from explicitly modelling the turbulent flow through the wind farm. This approach differs much compared to the statistical wind power forecast model mentioned before. By having the ability to use an atmospheric model which explicitly resolves flow through the wind farm, only the first part of high resolution metocean modelling is covered. However, the offshore community already has the ability to use a high resolution wave model, SWAN (Booij et al., 1999). Because of the close relation between wave growth and wind, this model is highly dependent on the skill performance of its provided wind fields. Usually, these wind fields are obtained via GCMs, but it should be more beneficial if SWAN were to be provided with high resolution wind fields (van Laerhoven, 2016), preferably via an atmospheric LES. A number of studies were performed using a higher resolution atmospheric model, coupled to a spectral wave model, e.g. Liu et al. (2011). However, these studies were performed using atmospheric models which still do not have the resolution to account for heterogenic effects. A benefit of an atmospheric LES is that it provides the resolution to account for these effects. If the atmospheric LES does not only provide its wind fields to SWAN, but it also receives feedback from the wave model, a realistic representation should arise of the offshore conditions. In this study, a similar approach as in Janssen et al. (2002) was followed.

1-4   Research objective and scope

In the previous section, the problems and advancements in numerical weather prediction were outlined. In this thesis, extension of the mentioned LES and SWAN studies is provided. More specifically, to study the interaction between the two models, which emerges in the roughness length, and its impact on wave modelling. The objective of this research is therefore to asses and advance modelling of the local sea state and roughness length in offshore wind farms by using an atmospheric large-eddy simulation coupled to a spectral wave model. Hence, the objective of this research can be formulated as follows:

Assess and advance atmospheric large-eddy simulations coupled to a spectral wave model for enhanced operational metocean forecasting in offshore wind farms.

The steps that will be completed in order to realize the objective, is schematically presented in Figure 1-1. The list on the next page elaborates on the defined steps.
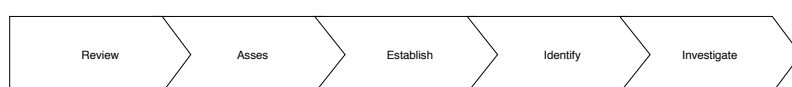
Figure 1-1: Schematic overview of thesis scope.

This research objective can be divided in the following tasks:

- Present a literature review on high resolution metocean modelling, focusing on atmospheric large-eddy simulations and spectral wave modelling and their interaction.

- Assessment of large-scale- and high-resolution atmospheric-/wave model performance. Purpose is to provide a benchmark in the area of study for the coupled simulations.

- Establish a method for coupling an atmospheric large-eddy simulation to a spectral wave model.

- Identify heterogenic effects on the sea state and roughness length.

- Investigate one- and two-way coupling of an atmospheric large-eddy simulation to a spectral wave model in a quantitative manner.

1-5   Structure of the report

In *Chapter 2* an introduction to the theoretical aspects of ocean waves is given. This chapter starts with a general description of waves, which will continue in providing the theoretical framework of spectral wave modelling, focusing on the wave generation by wind. Hereafter, the wave model used in this study is described.

Chapter 3 discusses some theoretical background of atmospheric large-eddy simulations. This chapter starts with a general description of the atmospheric boundary layer, hereafter atmospheric modelling is treated and continues in describing large-eddy simulations. Now sufficient knowledge is in place to connect the two theories. Therefore, interaction of the atmosphere and waves trough the roughness length is also discussed in this chapter.

Chapter 4 elaborates on the area where this research is performed. First, an introduction of the wind farm area is provided. Hereafter, the choice of the simulation domains is further explained. Also, the site conditions concerning bathymetry, wind and waves are presented.

Chapter 5 elaborates on the set-up of the simulations. All selected input data, pre-processing, simulation domains, set-ups, post-processing and analysis is discussed in detail.

Chapter 6 includes the simulation results and elaborates not only on the impact of the models concerning their performance but also on possible heterogenic effects. Furthermore, the simulation limitations are discussed

Lastly, *Chapter 7* concludes on the obtained insights of the simulations and continues in providing recommendations for future research and other application areas where high-resolution atmosphere-wave modelling could be an interesting opportunity.

Chapter 2

Waves

2-1 Introduction

This chapter discusses the theoretical framework needed to understand the wave simulations used in this research. The chapter starts with a general description of waves. Hereafter, the energy balance equation for oceanic and coastal water is discussed. Finally, the spectral wave model used in this research is treated. A considerable part of this chapter is based on theories presented in Holthuijsen (2007).

By looking at the ocean surface, one can see many different waves each travelling in its own direction, creating a chaotic pattern. Ocean waves are mostly generated by wind, but many other forms of wave generation occur. This is represented in Figure 2-1. Here, the energy of different regimes of waves are presented in relation to their frequency and period.
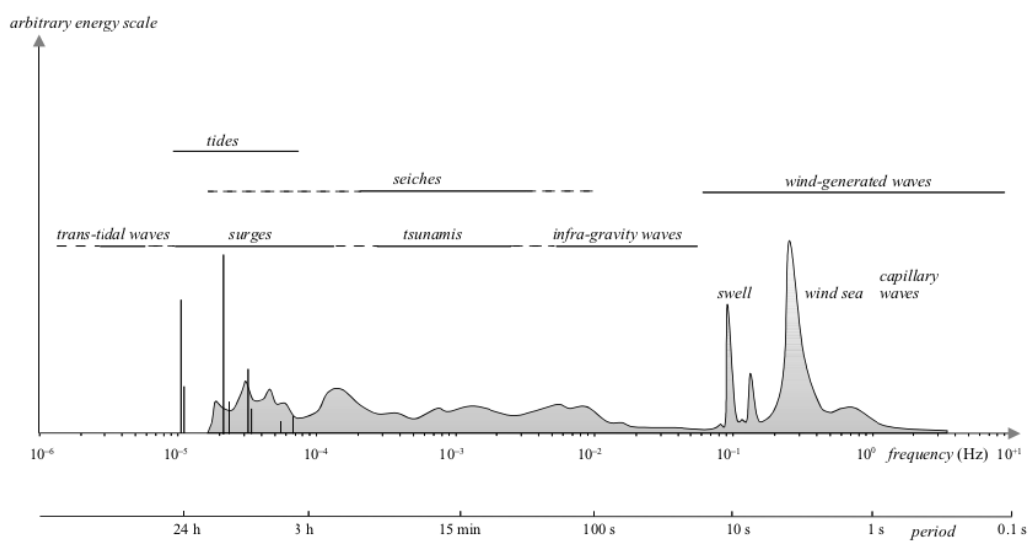
Figure 2-1: Typical ocean wave spectrum (Holthuijsen, 2007).

The wind-generated wave regime is the dominant contribution to the wave energy spectrum, because high amounts of energy are present in the frequency range of 0.04-4 Hz. As stated by van der Meulen (2012), the wind-generated wave regime can be categorized into three types of waves:

- **Swell**, wind waves which have left the generation area, typically long wave length.

- **Wind sea**, is created by the force on the sea surface which is exerted by wind .

- **Capillary waves**, small amplitude waves which are formed instantaneous (ripples).

These three wind-generated wave categories could also form groups which results in periodical infra-gravity waves. Furthermore, low frequency waves consist of tides and storm surges. Where tides are created by the gravitational force of the moon, sun and rotation of the earth, storm surges could result in a local sea level rise.

2-2   Description of waves

To describe a sea surface, one has to start with a regular harmonic wave. Many of these independent harmonic waves together, each with their own amplitude and frequency, create a realistic irregular sea surface. This is described by the random-phase/amplitude model, but this model would be enhanced if also the propagation direction of each of these harmonic waves is included. This represented in Figure 2-2.
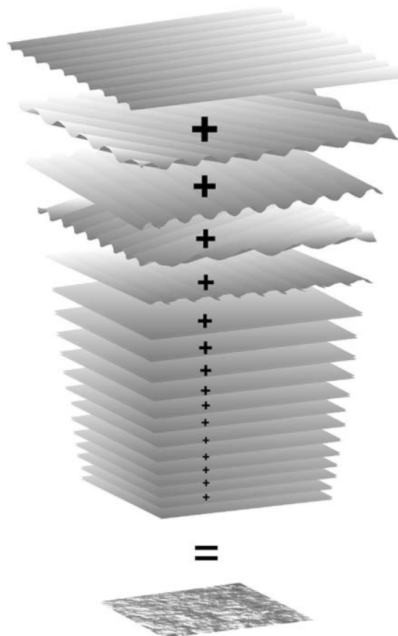
Figure 2-2: Superposition of many regular waves, creating an irregular sea surface (Pierson et al., 1955; Holthuijsen, 2007).

2-2-1 The frequency wave spectrum

To start with, an undirectional regular wave is considered which has a surface elevation as a function of time:

$$\eta(t) = a\cos\left(2\pi f t + \alpha\right) \tag{2-1}$$

Here, a is the amplitude, f is the frequency and α is the phase of the wave. However, to obtain the more realistic irregular wave model, one has to consider the summation of a large number of harmonic waves. This is denoted as the random-phase/amplitude model:

$$\eta(t) = \sum_{i=1}^{N} \underline{a}_i \cos\left(2\pi f_i t + \underline{\alpha}_i\right) \tag{2-2}$$

where N is a larger number of frequencies, the underscores indicate that the amplitude and phase of the wave are now random variables.

The amplitude is defined by the variance density spectrum (wave energy spectrum). Here, the expected value of the variance ($E\{\frac{1}{2}\underline{a}_i^2\}$) is considered instead of the expectation value of the amplitude ($E\{\underline{a}_i\}$). The reason for this is twofold. First, the variance is often used as a statistical quantity. Second, the energy of a wave is proportional to the variance. Furthermore, the wave variance density spectrum can be transformed into a continuous version instead of a discrete. This is necessary to represent all frequencies present at sea. To do so, the limit case is considered in which the frequency interval approaches zero. The variance density spectrum is defined as:

$$E(f) = \lim_{\Delta f \to 0} \frac{1}{\Delta f} E\left\{\frac{1}{2}\underline{a}^2\right\} \tag{2-3}$$

2-2-2 The frequency-direction wave spectrum

The one-dimensional variance density spectrum described above, characterises the time dependent surface elevation at one geographic location. To describe the three-dimensional variance density spectrum, the surface elevation function has to be expanded such that the x and y coordinates are included:

$$\eta(x, y, t) = a\cos\left(\omega t - kx\cos\theta - ky\sin\theta + \alpha\right) \tag{2-4}$$

where $\omega = 2\pi f$ and $k = 2\pi/L_{wave}$, in which L_{wave} is the wave length. The three-dimensional random-phase/amplitude model is the sum of all propagating harmonic waves:

$$\underline{\eta}(x, y, t) = \sum_{i=1}^{N}\sum_{j=1}^{M} \underline{a}_{i,j} \cos\left(\omega_i t - k_i x\cos\theta_j - k_i y\sin\theta_j + \underline{\alpha}_{i,j}\right) \tag{2-5}$$

Here, the wave number k_i and angular frequency ω_i are related by the dispersion relation and therefore are indicated by the same index i. The index j defines the discretized propagation

directions. Now, the discrete two-dimensional variance density spectrum can be transformed into a continuous wave energy spectrum:

$$E(f, \theta) = \lim_{\Delta f \to 0} \lim_{\Delta \theta \to 0} \frac{1}{\Delta f \Delta \theta} E \left\{ \frac{1}{2} \underline{a}^2 \right\} \tag{2-6}$$

If Equation 2-6 is integrated with respect to the direction θ_{wave} from 0 to 2π, Equation 2-3 is again obtained. The two-dimensional frequency-direction spectrum is however difficult to observe. Often, only overall directional parameters are observed i.e. the mean wave direction and the wave spectral directional width of the wave energy spectrum. This wave spectral directional width can be used to construct the directional distribution $D(f, \theta)$. It is defined as the cross-section of the normalized two-dimensional wave energy spectrum at a specific frequency:

$$E(f, \theta) = D(\theta; f) E(f) = D(\theta) E(f) \tag{2-7}$$

The shape of the directional distribution can be approximated by the following generalized model:

$$D(\theta) = \begin{cases} A_1 \cos^m \theta, & \text{for } |\theta| \leq 90° \\ 0, & \text{for } |\theta| > 90° \end{cases} \tag{2-8}$$

where the coefficient A_1 is given by the following function:

$$A_1 = \frac{\Gamma(\frac{1}{2}m + 1)}{\Gamma(\frac{1}{2}m + \frac{1}{2})\sqrt{\pi}} \tag{2-9}$$

Here, Γ is the gamma function and the power m in both equations controls the width of the distribution. According to Deltares (personal communication), it is approximated by the following relation:

$$m = \frac{2w}{1 - w} \tag{2-10}$$

where w is the wave spectral directional width. Furthermore, extreme values of the wave spectral directional width are capped by the following condition:

$$w = \min(w, 0.975) \tag{2-11}$$

2-2-3   Statistical characteristics

Because the wave spectrum contains many harmonic wave each with different phases and amplitudes, the wave crests and troughs all occur on different levels. Furthermore, every harmonic wave has their own wave period. Therefore, it is more convenient to define the

significant wave height H_s because of its better agreement with observations. The significant wave height is defined as the highest one-third of the waves:

$$H_s = H_{1/3} = \frac{1}{N/3} \sum_{j=1}^{N/3} H_j \tag{2-12}$$

Here, j is the rank number of the wave component, based on its height. Moreover, statistical characteristics can be estimated by the wave energy spectrum, including the significant wave height. These characteristics are described by the moments of the wave energy spectrum:

$$m_n = \int_0^\infty f^n E(f) df \tag{2-13}$$

Where the estimated significant wave height is described by:

$$H_{m_0} \approx 4\sqrt{m_0} \tag{2-14}$$

In Section 3-5, the wave period is considered. Here, the peak wave period, which is the corresponding frequency value of the highest bin in the frequency wave spectrum, is replaced by the mean absolute wave period (T_{m-10}). This is done to give more weight to lower frequency waves, it is defined as:

$$T_{m-10} = \frac{m_{-1}}{m_0} \tag{2-15}$$

2-3   Wave modelling

In order to introduce wave modelling for arbitrary cases (not idealized spectral shapes), the random-phase/amplitude model is again considered. Wave prediction is based on predicting each of the harmonic wave components in the random-phase/amplitude model. This means that the energy spectrum $E(f,\theta)$ of each component is considered as it varies in time and space. Therefore the spectrum is not only dependent on frequency and direction, but also on time and space:

$$E(f,\theta) = E(f,\theta; x, y, t) \tag{2-16}$$

Wave modelling consists of following each of these individual wave components in time and space, accounting for all effects of generation, dissipation and interaction encountered in its path.

2-3-1 Energy balance equation in deep waters

In deep waters, when the waves are less affected by the bottom, the evolution of the energy spectrum of each individual wave component $E(f, \theta)$ is obtained via the evolution equation of a wave ray:

$$\frac{dE(f, \theta; x, y, t)}{dt} = S(f, \theta; x, y, t) \tag{2-17}$$

Here, the left-hand term is the rate of change of the wave energy spectrum and $\partial x/\partial t = c_{g,x}$ and $\partial y/\partial t = c_{g,y}$ represent the group velocities in their respective direction. The right-hand term represents the source term and contains all the effects of generation, wave-wave interaction and dissipation.

For deriving a wave energy balance, consider a cell with grid sizes Δx and Δy. The wave energy balance is obtained by following a wave component $E(f, \theta)$ through this cell, the change of wave energy in the cell over a time interval is influenced by net wave energy import and generation/dissipation of wave energy in the cell. Following the derivation in Holthuijsen (2007), the energy balance equation in deep waters is obtained:

$$\frac{\partial E(f, \theta; x, y, t)}{\partial t} + \frac{\partial c_{g,x} E(f, \theta; x, y, t)}{\partial x} + \frac{\partial c_{g,y} E(f, \theta; x, y, t)}{\partial y} = S(f, \theta; x, y, t) \tag{2-18}$$

where $c_{g,x} = \partial x/\partial t$ and $c_{g,y} = \partial y/\partial t$ represent the group velocity in the x- and y-direction respectively. For deep waters, the source term on the right-hand consists of three elements:

$$S(f, \theta; x, y, t) = S(f, \theta) = S_{in}(f, \theta) + S_{nl4}(f, \theta) + S_{wc}(f, \theta) \tag{2-19}$$

The first term in Equation 2-19 (S_{in}) represents the process of wave generation by wind. It consists of two elements, which is given by:

$$S_{in}(f, \theta) = \underbrace{\alpha}_{\text{initial wave growth}} + \underbrace{\beta E(f, \theta)}_{\text{wave-induced wind-wave growth}} \tag{2-20}$$

The first element compromises the initial generation of waves. Here, waves are generated by resonance between propagating wind-induced pressure waves (air pressure) at the water surface and freely propagating water waves (Phillips, 1957). This initial generation is represented by the expression of Cavaleri and Rizzoli (1981):

$$S_{in,1}(f, \theta) = \alpha \tag{2-21}$$

where α is given by:

$$\alpha = \begin{cases} C_\alpha [u_* \cos(\theta - \theta_{wind})]^4, & \text{for } |\theta - \theta_{wind}| \leq 90° \\ 0, & \text{for } |\theta - \theta_{wind}| > 90° \end{cases} \tag{2-22}$$

Here, C_α is a tunable coefficient, u_* is the friction velocity and θ_{wind} is the wind direction. However, the second element represent the fact that the waves themselves also influence the wind-induced surface pressure. This is because the wind profile above the water surface will be disturbed by the wave, which decreases at higher elevations. The air pressure at the water surface is maximal on the windward side of the wave crest, minimal on the leeward side of the wave crest. Resulting in the fact that the wind pushes the water surface down on the windward side and moving the water surface up on the leeward side (Miles, 1957). This process is enhanced as the wave grows. The process described above is given by:

$$S_{in,2}(f,\theta) = \beta E(f,\theta) \tag{2-23}$$

where β is given by Snyder et al. (1981):

$$\beta = \epsilon \frac{\rho_a}{\rho_w} \left[28 \frac{u_*}{c} \cos\left(\theta - \theta_{wind}\right) - 1 \right] 2\pi f \tag{2-24}$$

Here, ϵ is a tunable coefficient, ρ_a is the air density, ρ_w is the water density and c is the phase speed of the wave component.
The other terms in Equation 2-19 (S_{nl4} & S_{wc}) represent the processes of wave-wave interaction. Where the second term includes the effect of nonlinear wave-wave interaction by quadruplet wave-wave interaction (S_{nl4}), which is the transfer of energy between waves by resonance. The third term includes the effect of dissipation by white-capping (S_{wc}), which is wave breaking in deep water. Because of the scope of this research, more information about these source terms can be found in Holthuijsen (2007).

2-3-2   Energy balance equation in shallow waters

The expression of the energy balance equation in shallow waters is derived in the same way as for deep waters. However, propagation of wave energy also needs to account for shoaling, refraction and diffraction. Also, the number of source or sink terms is more as in deep waters. For example, bottom friction is an additional sink term present in coastal waters.
In the energy balance equation for shallow waters, the depth-dependent group velocity already accounts for shoaling. Refraction and diffraction require an extra propagation term in the energy balance equation. Because if an individual wave component travels through a shallow water region, refraction and diffraction affect the propagation direction of the wave component. This additional term in the energy balance equation therefore accounts for this change of propagation direction. Again, following the derivation in Holthuijsen (2007), the energy balance equation in shallow waters is obtained:

$$\frac{\partial E(f,\theta;x,y,t)}{\partial t} + \frac{\partial c_{g,x}E(f,\theta;x,y,t)}{\partial x} + \frac{\partial c_{g,y}E(f,\theta;x,y,t)}{\partial y}$$
$$+ \frac{\partial c_\theta E(f,\theta;x,y,t)}{\partial \theta} = S(f,\theta;x,y,t) \tag{2-25}$$

where $c_{g,x}$ and $c_{g,y}$ represent the depth-dependent group velocities, c_θ represents the refraction- or diffraction-induced turning rate of the individual wave components. For shallow waters, the source term on the right-hand can be divided into three terms:

$$S(f, \theta; x, y, t) = S(f, \theta) = S_{in}(f, \theta) + S_{nl}(f, \theta) + S_{diss}(f, \theta) \tag{2-26}$$

The first term in Equation 2-26 (S_{in}) again represents the process of wave generation by wind (see Section 2-3-1). The second term (S_{nl}) represent nonlinear wave-wave interactions. It consists of two elements:

$$S_{nl}(f, \theta) = S_{nl3}(f, \theta) + S_{nl4}(f, \theta) \tag{2-27}$$

Next to nonlinear wave-wave interaction by quadruplet wave-wave interaction (S_{nl4}) which fulfill the resonance condition for four wave components, triad wave-wave interaction (S_{nl3}) also occurs in shallow water. It consist of the resonance conditions for three wave components. The third term in Equation 2-26 (S_{diss}) represents dissipation. It consists of three elements:

$$S_{diss}(f, \theta) = S_{wc}(f, \theta) + S_{bfr}(f, \theta) + S_{surf}(f, \theta) \tag{2-28}$$

Next to white capping (S_{wc}) discussed in the previous section, dissipation also includes bottom friction (S_{bfr}) and surf-breaking (S_{surf}), which represents the depth-induced wave breaking. Because of the scope of this research, more information about the definitions and corresponding expressions of these source terms can be found in Holthuijsen (2007).

2-3-3   Spectral wave model

The spectral wave model used for this study is called the SWAN wave model (Booij et al., 1999). SWAN is a third-generation spectral wave model developed at the Delft University of Technology that is specifically designed for coastal applications. Furthermore, the model is open-source and based on the theories described in this chapter. It is widely used by scientists and engineers for wave related research and consultancy (SWAN, 2019).
The model solves the spectral action balance equation or, in case wave-current interactions are disregarded as in this study, the spectral energy balance equation. It incorporates formulations for deep water processes of wave generation, dissipation and quadruplet wave-wave interactions. Specific shallow water formulations are used for dissipation due to bottom friction, triad wave-wave interactions and depth-induced breaking. The formulations for deep water processes are identical to those of the WAM wave spectral model, incorporated in the general circulation model of ECMWF.

Chapter 3

Atmosphere

3-1 Introduction

This chapter discusses the theoretical framework needed to understand the atmospheric simulations used in this study. The chapter starts with a general description of the atmospheric processes. After this is discussed, the chapter continuous in describing atmospheric modelling in general and large-eddy simulations more specifically.

3-2 Atmospheric boundary layer

The earth's atmosphere consists of several layers, where the troposphere is the lowest one. The boundary of this layer is the earth's surface. Transport processes at this boundary modify the lowest 100 to 3000 meters of the troposphere, creating what is called the atmospheric boundary layer (ABL). The remainder of the air in the troposphere is called the free atmosphere (Stull, 1988).

3-2-1 Turbulence

The wind speed in the ABL varies from zero, at the ground, to approximately the geostrophic wind. This phenomenon is described as wind shear. Wind shear, in its turn, is greatly dependent on the atmospheric stability (Section 3-2-2), which is the tendency for air parcels to ascent and mix with its environment. Locally however, the flow of air parcels is dominated by turbulence. It is know as the deviation from the mean flow of given parameter, moving randomly in vortex-like structures called eddies. A procedure known as Reynolds-averaging illustrates this by splitting the time signals of the horizontal- and vertical wind speeds in a mean and turbulent part:

$$u(t) = \overline{u} + u'(t) \tag{3-1}$$

$$w(t) = \overline{w} + w'(t) \tag{3-2}$$

The overbars are time averages and the primes are the deviating components. Transport of momentum in the vertical direction is computed by the vertical momentum flux:

$$\begin{aligned}
\overline{uw} &= \overline{(\overline{u} + u')(\overline{w} + w')} \\
&= \overline{\overline{u}\overline{w}} + \overline{\overline{u}w'} + \overline{u'\overline{w}} + \overline{u'w'} \\
&= \overline{u}\overline{w} + \overline{u'w'}
\end{aligned} \tag{3-3}$$

Equation 3-3 shows that that momentum is transported as a function of time, partly by mean flow and partly by turbulent flow.

3-2-2 Stability

To describe the state of the atmospheric boundary layer, the atmospheric stability is considered. The atmospheric stability is described best by using the potential temperature term, instead of the absolute temperature.
Consider a parcel of air (assume its an ideal gas), where its absolute temperature is dependent on the air pressure:

$$T = \rho R_d p \tag{3-4}$$

where ρ is the air density, R_d is the gas constant of dry air and p is the air pressure. If the air parcel rises in altitude, the pressure decreases and consequently the temperature of the parcel decreases according to Equation 3-4. The potential temperature accounts for this change in temperature:

$$\theta = T \left(\frac{p_0}{p} \right)^{R/c_p} \tag{3-5}$$

where θ is the potential temperature, T is the absolute temperature, p_0 is the reference pressure, p is the pressure of the air parcel, R is the gas constant and c_p is the specific heat capacity. Furthermore, according to Holtslag (2016), humidity also has an influence on an air parcel. Water vapour has a molar mass of 18 g mol^{-1}, dry air (mixture of mostly nitrogen and oxygen) has a molar mass of 29 g mol^{-1} (de Roode, 2019). Therefore, if more water vapour is added to the air, the molar mass is reduced. Thus, a humid air parcel is lighter than its environment if both are at constant temperature and pressure. Assuming the air is not saturated, the virtual potential temperature also accounts for humidity effects:

$$\theta_v = \theta[1 + 0.61r] \tag{3-6}$$

where r is the mixing ratio, which stands for the mass ratio of water vapour and dry air. Especially for offshore conditions, the virtual potential temperature is of great use because of its abundance of water ready for evaporation.
As stated by Holtslag (2016), three different regions of the state of the atmosphere can be defined as a function of its temperature profile:

- Increase of virtual potential temperature with height ($d\theta_v/dz > 0$). If the air parcel ascends, it will be cooler than its environment and therefore heavier than its environment. This will result in the parcel to descend due to gravity. Here, vertical motions are suppressed by buoyancy effects. This is defined as a **stable** atmosphere.

- Constant virtual potential temperature with height ($d\theta_v/dz = 0$). If the air parcel ascends, it will be the same temperature as its environment. Without forcing, it will continue to ascend at the same speed. This is defined as a **neutral** atmosphere.

- Decrease of virtual potential temperature with height ($d\theta_v/dz < 0$). If the air parcel ascends, it will be warmer than its environment and therefore lighter than its environment. This will result in the air parcel to accelerate upwards and the heavier environment to descend. Here, vertical motions are enhanced by buoyancy effects. This is defined as an **unstable** atmosphere.
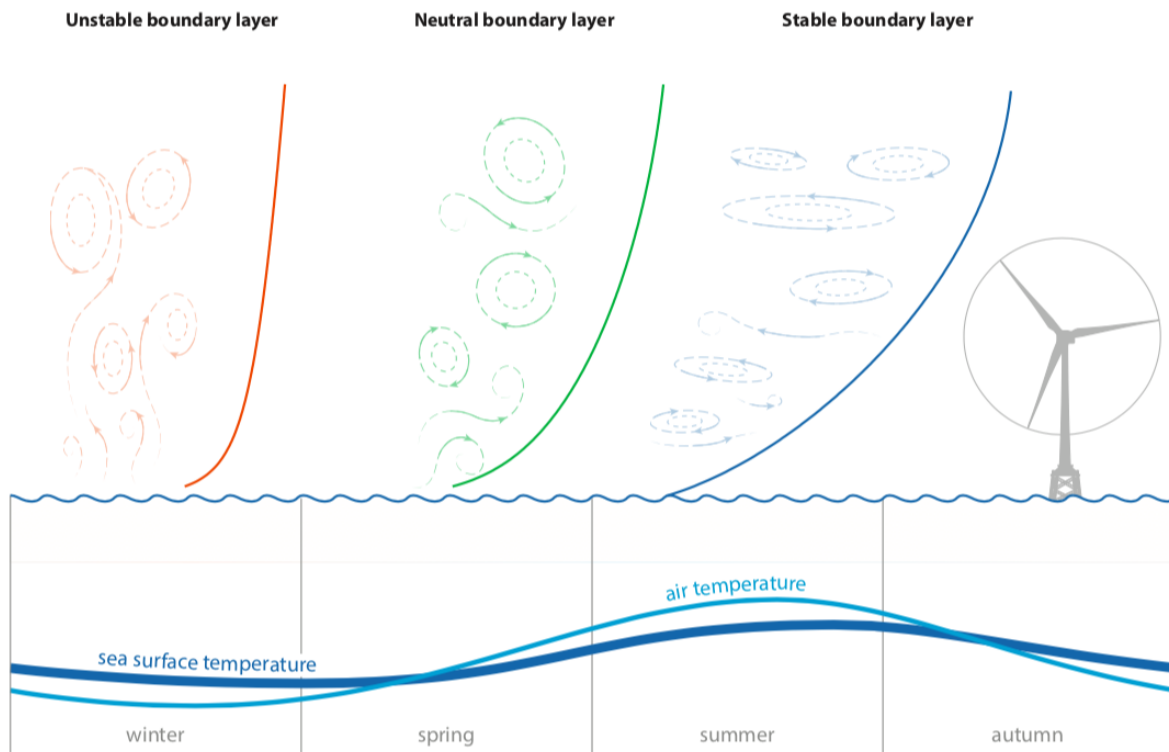
Figure 3-1: Offshore wind profile (solid vertical line) under the influence of atmospheric stability (Holtslag, 2016).

The atmospheric stability is a crucial term in this research, because it is necessary to understand the different stability regimes discussed later in this chapter. Furthermore, stability plays a role in coupled atmosphere-sea simulations because of its ties to the roughness length z_0, which is discussed further in Section 3-5. To characterize the stability of the atmosphere, often the Obukhov length L is considered. The Obukhov length (Obukhov, 1971) is defined as a length scale that represents at which height convection driven turbulence starts to dominate over shear produced turbulence. Its length is defined by:

$$L = -\frac{\theta_v u_*^3}{g\kappa\overline{w'\theta_v'}} \tag{3-7}$$

where θ_v is the virtual potential temperature, u_* the friction velocity, g the gravitational acceleration, κ is the Von Kármán constant and $\overline{w'\theta_v'}$ is the virtual potential temperature flux. The Obukhov length is often used in its dimensionless form: $\zeta = z/L$, also known as the dimensionless stability parameter.

3-3   Atmospheric modelling

In the previous section, an introduction to atmospheric boundary layer meteorology was given with the focus on atmospheric stability and turbulence. However, in order to use this physics for weather- and climate forecasting, one needs to consider atmospheric modelling. Numerical simulation is the only way to predict behaviour in the atmospheric boundary layer. The general approach to such a numerical simulation, better known as a numerical weather prediction (NWP), is to divide the domain of the simulation into control volumes called grid cells. The physical processes effecting each cell are computed for each time step, as well as interactions with neighboring cells.

The idea to model the weather by using numerical approximation was pioneered by Richardson (1922). However, this idea had to wait until the mid fifties for the first digital computers, to perform the first successful numerical weather forecast.

The reason for the necessity of computing power for atmospheric modelling is because the atmosphere is a very complex system of different physical processes, all interaction with each other. Besides, these processes operate on scales ranging from the millimeter to the planetary scale. Furthermore, processes at all these different motion scales interact with each other. To obtain an exact solution, motion on all these scales must be resolved, which is obviously not possible at this time.

Nevertheless, solutions can be approximated when we use the above mentioned grid cells. The scales of motion that can be resolved are consistent with the number of these grid cells used. The higher or lower scales are represented in a statistical way. This representation for missing scales are called parameterizations. Depending on the type of model, processes are more relevant or irrelevant. Generally, each atmospheric model concerns the motion of wind, pressure, temperature and density. Thus, with limited computing resources, a trade-off between resolution and domain size needs to be considered. As stated by Schalkwijk (2015), the spectrum of atmospheric models can be categorized by the resolution of their grid cells:

- **General circulation models** (GCMs) simulate the weather over the entire globe and form the backbone of weather and climate modelling. Smaller atmospheric motions must be parameterized.

- **Limited-area models** (LAM) lie between LES (see below) and GCMs. LAM covers a broad range of different models, ranging from heavily parameterized circulation models on a relative small domain to LES models adapted to model large-scale weather and climate phenomena. A typical example are meso-scale models, where the Weather Research and Forecasting model (WRF) is a commonly used one.

- **Large-eddy simulations** (LES) parameterize only the smallest scales of turbulence. LES models are able to simulate the turbulent scales containing the most energy.

- **Direct numerical simulations** (DNS) models feature no parameterization, it solves all scales of turbulence. Therefore it is very computationally expensive and only used for a very small domain.

When computing power increases, the number of grid cells can be increased. This should result in resolving more scales of motion, which reduces the amount of parameterizations and eventually this should further enhance the model accordingly.

3-3-1 Governing equations

In a numerical weather prediction model, a set of equations describing atmospheric flow is solved. As stated by Hintz (2016), these equations are known as governing equations which consists of the continuity equation, the equation of motion, the equation for conservation of moisture and the equation for conservation of energy. In this section, the Reynold averaged Navier-Stokes (RANS) equation is first considered to provide a basic insight into modelling atmospheric turbulent flows. Section 3-4 continues in describing large-eddy simulations which can explicitly resolve turbulent processes. Because the focus of this research is mainly on the interaction of atmospheric flow with waves, only the equation of motion is considered. For the reason that the Navier-stokes equation is difficult to solve analytically, Reynolds averaged atmospheric models (GCMs) decompose the physical variables into a mean part ($\overline{u}_i$) and turbulent part (u_i'), as can be seen in Section 3-2-1. By following the derivation in Hintz (2016), the Reynolds averaged Navier-Stokes equation is obtained:

$$\underbrace{\frac{\partial \overline{u}_i}{\partial t}}_{\text{rate of change}} = - \underbrace{\frac{\overline{u}_j \partial \overline{u}_i}{\partial x_j}}_{\text{advection}} - \underbrace{\delta_{i3} g}_{\text{gravity}} + \underbrace{\epsilon_{ij3} f_c \overline{u}_j}_{\text{Coriolis force}} - \underbrace{\frac{1}{\rho} \frac{\partial \overline{p}}{\partial x_i}}_{\text{pressure gradient}}$$
$$+ \underbrace{\nu \frac{\partial^2 \overline{u}_i}{\partial x_j^2}}_{\text{viscous stress}} - \underbrace{\frac{\partial (\overline{u_j' u_i'})}{\partial x_j}}_{\text{Reynolds stress}} \tag{3-8}$$

The last term of the Reynolds averaged Navier-Stokes equation, Reynolds stress term, can also be written as:

$$\frac{\partial (\overline{u_j' u_i'})}{\partial x_j} = \frac{1}{\rho} \frac{\partial \tau_{ij}}{\partial x_j} \tag{3-9}$$

where the Reynolds stress tensor is given by:

$$\tau_{ij} = -\rho \overline{u_j' u_i'} \tag{3-10}$$

However, Equation 3-8 is the expression for the mean velocity, but it is still dependent on the turbulent term, which is unknown. Therefore, in order to describe the behaviour of the mean

velocity, knowledge on turbulence is needed. A possible solution is to parameterize the flux of a variable ξ via the gradient of ξ times an eddy diffusivity coefficient K:

$$\overline{u'_j \xi'} = -K \frac{\partial \overline{\xi}}{\partial x_j} \tag{3-11}$$

For vertical momentum transfer, when flow in the u_1 is considered, the following expression is obtained:

$$\overline{u'w'} = -K_m \frac{d\overline{u}}{dz} \tag{3-12}$$

3-3-2   Monin-Obukhov similarity theory

Consider the Reynolds averaged Navier-Stokes equation (Equation 3-8). Following the assumptions made in Hintz (2016), were all therms of the equation are zero except for the turbulent momentum flux when $j = 3$. The flow is aligned to the u_1 direction:

$$\frac{\partial \overline{u'w'}}{\partial z} = 0 \quad \Rightarrow \quad -\overline{u'w'} = \text{const} \tag{3-13}$$

The vertical momentum flux can be used to define the friction velocity u_*:

$$u_*^2 = \tau/\rho = -\overline{u'w'} \tag{3-14}$$

where τ is the shear stress and ρ the density of air. Following the derivation in Monin and Obukhov (1954) an expression for the averaged x-component of the wind gradient is obtained:

$$\frac{d\overline{u}}{dz} = \frac{u_*}{\kappa z} \tag{3-15}$$

Monin and Obukhov (1954) evaluated the wind gradient above by making it non-dimensional with the length scale z and velocity scale u_*:

$$\frac{\kappa z}{u_*} \frac{\partial \overline{u}}{\partial z} \tag{3-16}$$

where κ is the Von Kármán constant. This non-dimensional term should be in its turn a function of the dimensionless stability parameter ζ:

$$\frac{\kappa z}{u_*} \frac{d\overline{u}}{dz} = \phi_m(\zeta) \tag{3-17}$$

Here, ϕ_m is the stability function of momentum. By rewriting Equation 3-17, the gradient in the vertical direction of the averaged x-component of wind is obtained:

$$\frac{d\overline{u}}{dz} = \frac{u_*}{\kappa z}\phi_m(\zeta) \tag{3-18}$$

In this research different stability functions for stable conditions (Högström, 1988) and unstable conditions (Wilson, 2001) are used:

$$\phi_m = \begin{cases} 1 + \beta\zeta, & \text{for } \zeta > 0 \quad \text{(Stable)} \\ 1, & \text{for } \zeta = 0 \quad \text{(Neutral)} \\ (1 + \gamma|\zeta|^{2/3})^{-1/2}, & \text{for } \zeta < 0 \quad \text{(Unstable)} \end{cases} \tag{3-19}$$

This wind gradient expression could be used to determine the diffusivity coefficient in Equation 3-11. However, it is also used to evaluate a wind velocity profile in the atmospheric boundary layer. It is obtained by integrating the wind gradient from z_0 to z:

$$\overline{u}(z) = \frac{u_*}{\kappa} \int_{z_0}^{z} \frac{\phi_m}{z} dz \tag{3-20}$$

After integration, the general definition for the logarithmic profile for the x-component of wind is acquired:

$$\overline{u}(z) = \frac{u_*}{\kappa} \left[\ln\left(\frac{z}{z_0}\right) + \Psi_m(\zeta) \right] \tag{3-21}$$

with the integrated stability functions:

$$\Psi_m(\zeta) = \begin{cases} \beta(\zeta - \zeta_0), & \text{for } \zeta > 0 \quad \text{(Stable)} \\ 0, & \text{for } \zeta = 0 \quad \text{(Neutral)} \\ -3\ln\left(\frac{1+\sqrt{1+\gamma_m|\zeta|^{2/3}}}{1+\sqrt{1+\gamma_m|\zeta_0|^{2/3}}}\right), & \text{for } \zeta < 0 \quad \text{(Unstable)} \end{cases} \tag{3-22}$$

Both γ and β are empirical parameters. According to Högström (1988) and Wilson (2001), $\beta = 4.8$ and $\gamma_m = 3.6$.
Now there is a theoretical framework to describe the wind profile in the ABL, as a function of the atmospheric stability and the roughness length. This is discussed further in Section 3-5.

3-4   Large-eddy simulations

In this research, large-eddy simulations are used to simulate atmospheric flow. These simulation were first formulated by Smagorinsky (1963), later explored by Deardorff (1970). As stated by van Laarhoven (2019), these simulations accurately resolve the large scale motions (large eddies) which contain the most kinetic energy, smaller scales are being parameterized. Hereby, domain size can be increased without compromising computing cost.
However, processes such as large scale pressure systems, are not resolved by the simulation. Because the domain lacks size for actively resolving the processes, this needs to be provided to the simulation by general circulation models (GCMs). Data obtained from a GCM is used

for the initial conditions and boundary values for the large-eddy simulation. In Section 5-2 these input data, obtained from the GCM, is discussed further.

The LES model used in this research is called the GPU-Resident Atmospheric Simulation Platform (GRASP). The code of GRASP is a further enhancement of the GPU-resident Atmospheric Large-Eddy Simulation (GALES). GALES originates from the Dutch Atmospheric Large-Eddy Simulation (DALES). Were DALES runs on central processing units (CPU), Schalkwijk et al. (2012) ported it to run completely on graphical processing units (GPU), which resulted in GALES. GPU-based codes enable high speed simulations, which make large-eddy simulations an attractive option for operational weather forecasting. Because of the implementation of wind turbines in the model (van Dorp, 2016), highly accurate power forecasting for offshore wind farms became one of its applications.

DALES is also still used an maintained by researchers of several universities and institutes including; Delft University of Technology (TUD), Wageningen University and Research (WUR) and the Royal Dutch Meteorological Institute (KNMI). It is described in detail by Heus et al. (2010).

3-4-1   Physics of large-eddy simulations

As described in the previous section, GRASP is an enhancement of DALES and GALES. But the physics is treated in the same way. The principle of a large-eddy simulation, in this case GRASP, is to apply a filter to the grid of the control volumes. Eddies larger than the filter width, with the most kinetic energy, are resolved. Eddies smaller than the filter width, with less kinetic energy, are parameterized by a subfilter-scale (SFS) model. Now the physical variables are not decomposed into a time-average and turbulent part as in RANS, but into a grid cell average part ($\widetilde{u_i}$) and subgrid part (u_i').

The prognostic variables in GRASP are the three velocity components u_i ($i = 1, 2, 3$), the liquid water potential temperature θ_l, the total (non-precipitating) specific humidity q_t and the precipitating water specific humidity q_r. Adding up these two specific humidity's gives the total amount of water, a micro-physics scheme implemented in GRASP is responsible for the conversion between q_t and q_r (Heus et al., 2010). The essential difference between the two is that q_t follows atmospheric flow, and q_r develops motion relative to the flow (precipiation). In a large-eddy simulation, a spatial filter is applied to these prognostic variables. These filtered variables are denoted with a tilde ($\widetilde{u_i}$). The continuity and LES-filtered momentum equations are therefore described by (Schalkwijk et al., 2014):

$$\frac{\partial \rho \widetilde{u_i}}{\partial x_i} = 0 \tag{3-23}$$

$$\underbrace{\frac{\partial \widetilde{u_i}}{\partial t}}_{\text{rate of change}} = - \underbrace{\frac{1}{\rho}\frac{\partial \rho \widetilde{u_i}\widetilde{u_j}}{\partial x_j}}_{\text{resolved advection}} - \underbrace{\frac{1}{\rho}\frac{\partial \rho \tau_{ij}}{\partial x_j}}_{\text{subgrid}}$$

$$- \underbrace{\frac{\partial \pi}{\partial x_i}}_{\text{pressure}} - \underbrace{\delta_{i3}g\frac{\tilde{\theta}_v - \langle\theta_v\rangle}{\langle\theta_v\rangle}}_{\text{buoyancy}} \tag{3-24}$$

$$+ \underbrace{\epsilon_{ij3}f_c\left(\widetilde{u_j} - U_j^{geo}\right)}_{\text{Coriolis \& large-scale pressure}} + \underbrace{F_i}_{\text{sources \& sinks}}$$

The first two terms represent turbulent transport of $\widetilde{u}_i$, on the resolved- and sub-filter scale. In the subgrid term, τ_{ij} represents the subgrid momentum flux, it is defined by:

$$\tau_{ij} = \widetilde{u_i u_j} - \widetilde{u}_i \widetilde{u}_j \tag{3-25}$$

However, the subgrid momentum flux is modelled in a similar way as in Section 3-3-1:

$$\tau_{ij} = -K_m \left(\frac{\partial \widetilde{u}_i}{\partial x_j} + \frac{\partial \widetilde{u}_j}{\partial x_i} \right) \tag{3-26}$$

The third term contains the gradient of the modified pressure $\pi = \tilde{p}'/\rho_0$, where $\tilde{p}' = \tilde{p} - p_e$ is the pressure difference with the environmental state. The fourth term represents the buoyancy forces acting on the system. Here, $\langle \theta_v \rangle$ indicates the horizontal slab average of the virtual potential temperature. Furthermore, rotation of the Earth and the driving pressure forces are accounted in the Coriolis and large-scale pressure term, the last term contains the sources and sinks in the domain.

Additional equations for transportation of atmospheric scalar fields are also included in GRASP. The conservation equation for a conserved variable $\phi \in \{\theta_l, q_t\}$ is given by the momentum equation (Schalkwijk, 2015):

$$\underbrace{\frac{\partial \widetilde{\phi}}{\partial t}}_{\text{rate of change}} = - \underbrace{\frac{1}{\rho} \frac{\partial \widetilde{u}_j \widetilde{\phi}}{\partial x_j}}_{\text{resolved advection}} - \underbrace{\frac{\partial R_{u_j,\phi}}{\partial x_j}}_{\text{subgrid}} + \underbrace{S_\phi}_{\text{sources}} \tag{3-27}$$

Again, the first two terms represent turbulent transport of the scalars on the resolved- and sub-filter scale. In the subgrid term, $R_{u_j,\phi}$ represents the sub-filter scale scalar fluxes and is defined as:

$$R_{u_j,\phi} = \widetilde{u_j \phi} - \widetilde{u}_j \widetilde{\phi} \tag{3-28}$$

However, the sub-filter scale scalar fluxes are also modelled through an eddy diffusivity:

$$R_{u_j,\phi} = -K_h \frac{\partial \widetilde{\phi}}{\partial x_j} \tag{3-29}$$

The last term in Equation 3-29, S_ϕ, contains the sources and sinks in the system of the specific scalar variables.

3-4-2   Surface model

GRASP requires a procedure to determine the momentum- and scalar fluxes at the bottom boundary, were the exchange between the ocean and atmosphere takes place, because GRASP does not resolve the flow up to the lowest level (see Figure 3-2). Equation 3-30 and 3-31 are both expressions for the averaged bulk Richardson number between the surface and the first

model level z_1. By equating these equations, the Obukhov length L (Equation 3-32), can be determined.

$$Ri_b = \frac{z_1}{L} \frac{\left[\ln\left(\frac{z_1}{z_{0h}}\right) - \Psi_H\left(\frac{z_1}{L}\right) + \Psi_H\left(\frac{z_{0h}}{L}\right)\right]}{\left[\ln\left(\frac{z_1}{z_0}\right) - \Psi_M\left(\frac{z_1}{L}\right) + \Psi_M\left(\frac{z_0}{L}\right)\right]^2} \tag{3-30}$$

$$Ri_b = \frac{g}{\theta_0} \frac{z_1(\langle \widetilde{\theta}_{v1} \rangle - \langle \widetilde{\theta}_{v0} \rangle)}{\langle U_1 \rangle^2} \tag{3-31}$$

$$L = -\frac{\langle \theta_{v0} \rangle u_*^3}{g\kappa \langle \widetilde{w'\theta'_{v0}} \rangle} \tag{3-32}$$

Here, z_0 and z_{0h} are the roughness lengths for momentum and heat, Ψ_H and Ψ_M are the integrated stability function discussed in Section 3-3-2, $\langle \widetilde{\theta_{v1}} \rangle$ and $\langle \widetilde{\theta_{v0}} \rangle$ are the spatially averaged filtered virtual potential temperature at the first model levels and surface, $\langle U_1 \rangle = \sqrt{\langle \widetilde{u}_1 \rangle^2 + \langle \widetilde{v}_1 \rangle^2}$ and $\langle \widetilde{w'\theta'_{v0}} \rangle$ is the averaged surface virtual potential temperature flux (Heus et al., 2010).

The Obukhov length is used for computing the friction velocity u_*, which in its turn is used in the expression for determining the subfilter-scale momentum fluxes. Where the subfilter-scale momentum flux along the u-component at the surface is given by:

$$\widetilde{u'w'}_0 = -\frac{u_*^2}{\langle U_1 \rangle} \widetilde{u_1} \tag{3-33}$$

The subfilter-scale momentum- and scalar fluxes for higher levels are fully determined by the subgrid terms in Equation 3-24 and 3-27. Both are modeled by Equation 3-26 and 3-29 respectively. As can be seen in Figure 3-2, the amount of subfilter eddies decreases at elevated model levels. This should result in a less significant subgrid term for higher model levels.
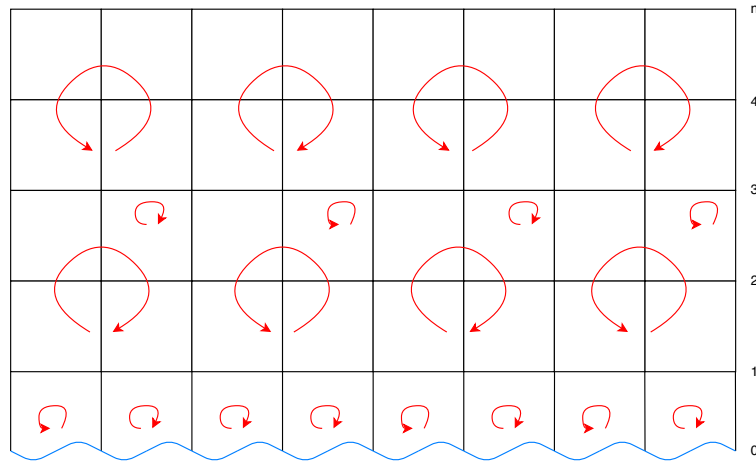
Figure 3-2: Schematic representation of eddy size and their typical occurrence in LES domain.

3-4-3   Wind turbine implementation

As mentioned in the introduction of this section, a wind turbine model was implemented in GRASP, which allows to accurately solve atmospheric flows in- and around wind farms. The wind turbine model presented in van Dorp (2016), the blade element theory, is unfortunately not very practical. This is because it is heavily dependent on the geometry of the blades and turbines, which is information that is often lacking. Therefore, a more simplistic model was implemented, but widely accepted as an accurate model to represent turbine far wakes and wake mixing (Allaerts and Meyers, 2017). In this research an actuator disk model (ADM) was used, similar to Meyers and Meneveau (2010), to represent the forcing of the wind turbine blades on the atmospheric flow. The actuator disk model, which represents the blades as a porous disk, computes the trust force of a single turbine:

$$F_{turbine} = \frac{1}{2}\rho C_T' U_d^2 \frac{\pi}{4} D^2 \tag{3-34}$$

where ρ is the density of air, U_d is the time-averaged disk-average axial velocity at the turbine, C_T' is the disk-based thrust coefficient and D is the rotor diameter.

3-5   Roughness length

As discussed in Section 3-3-2, the roughness length z_0 plays an important role in turbulence modelling in the atmospheric boundary layer through Monin-Obukhov similarity theory (MOST). It models the height where the wind velocity is equal to zero. Therefore, through the definition of the roughness length the surface roughness is defined, whether that be on land or at sea. This also emerges in the surface model of GRASP, discussed in Section 3-4-2, where the roughness length for momentum is necessary for computing the bulk Richardson number and the consequent friction velocity which represents the momentum transfer to the ocean surface.
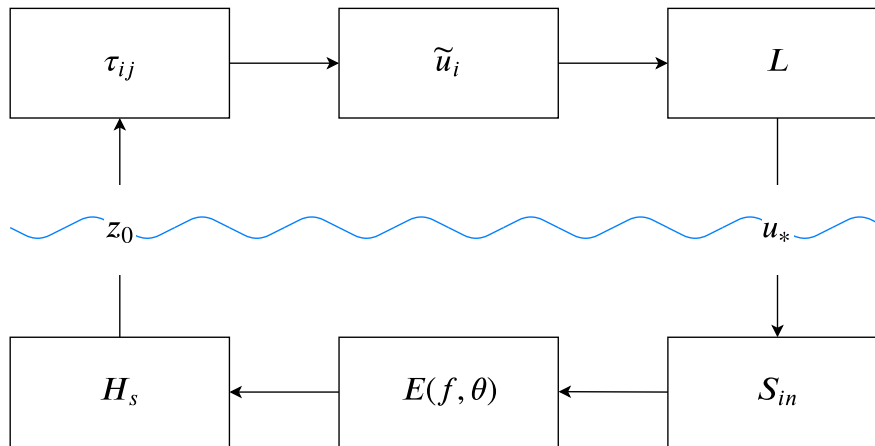
Figure 3-3: Schematic overview of momentum exchange between the ocean and atmosphere in a coupled GRASP/SWAN configuration.

In Figure 3-3, the general closed system of a coupled momentum exchange between the atmosphere and ocean is represented in a configuration where GRASP and SWAN are coupled. It starts with a resolved velocity component $\widetilde{u}_i$, through the evaluation of the Obukhov length L, the friction velocity u_* is computed. This results in generation of wind waves S_{in}, which causes a change to the wave energy spectrum and consequently to the sea state. Subsequently, this gives a different roughness length z_0, which influences the resolved velocity component again through the subgrid momentum flux τ_{ij}. In the next sections, two parametrizations of the roughness length for momentum are discussed.

3-5-1   Constant

Up until recently, the value for the roughness length that was implemented in GRASP was a constant over the entire domain. These constants are however different for each type of terrain. Typical values have been derived over the years, as can be seen in Table 3-1.

Table 3-1: Roughness lengths for different types of terrain, adapted from WMO (2008).

Terrain description	z_0 (m)
Open sea, fetch at least 5 km	0.0002
Mud flats, snow; no vegetation, no obstacles	0.005
Open flat terrain; grass, few isolated obstacles	0.03
Low crops, occasional large obstacles; $x/h > 20$	0.10
High crops, scattered obstacles, $15 < x/h < 20$	0.25
Parkland, bushes, numerous obstacles, $x/h \approx 10$	0.50
Regular large obstacle coverage (suburb, forest)	1.0
City centre with high- and low-rise buildings	≥ 2

Later, values for the roughness length were obtained via a GCM. However, these values still had a coarse resolution and were therefore not that appropriate to use in atmospheric large-eddy simulations.

3-5-2   Charnock (1955)

To provide a more realistic representation of the offshore conditions regarding the roughness length, the Charnock (1955) relation defines a more accurate method to express the roughness length:

$$z_0 = \alpha \frac{u_*^2}{g} \tag{3-35}$$

Charnock studied the wind profile under the influence of waves. By conducting measurements, a generalized wind profile for flow over a water surface was established. Here, α is the Charnock constant, different values can be found in Table 3-2.
For (uncoupled) atmospheric simulations, GRASP uses the Charnock relation to compute the roughness length. The Charnock constant implemented in GRASP is based on Wu (1980). However, the most realistic roughness lengths are obtained when its expression is dependent

on the sea state (i.e. significant wave height and/or the steepness of waves). In order to do so, an additional wave model must be coupled to GRASP in order to provide this dependency on the roughness length, this is discussed further in the next section.

Table 3-2: Charnock constant α obtained from literature, adapted from Garratt (1992).

#	Reference	α
1.	Charnock (1958)	0.012
2.	Kitaigorodskii and Volkov (1965)	0.035
3.	Wu (1969)	0.0156
4.	Clarke (1970)	0.032
5.	Smith and Banke (1975)	0.013
6.	Garratt (1977)	0.0144
7.	Wu (1980)	0.0185
8.	Geernaert et al. (1986)	0.0265

3-5-3 Taylor and Yelland (2001)

Taylor and Yelland (2001) proposed an alternative scaling which is fully dependent on the wave steepness:

$$\frac{z_0}{H_s} = A_1 \left(\frac{H_s}{L_p} \right)^{B_1} \tag{3-36}$$

with $A_1 = 1200$ and $B_1 = 4.5$. According to Drennan et al. (2005), this parameterization was found to well describe a variety of sea state conditions, with the exception of young waves. The peak wave length is computed using the dispersion relation:

$$L_p = \frac{gT_p^2}{2\pi} \tanh \left(\frac{2\pi d}{L_p} \right) \tag{3-37}$$

where T_p is the peak wave period. In this study, an alternative procedure was proposed for determining the peak wave period. Here, the mean absolute period (T_{m-10}) is considered, to give higher weight to lower frequency waves i.e. longer wave periods. A multiplication factor of 1.1 was added to T_{m-10} in order to shift the corresponding frequency to the peak frequency of the wave energy spectrum, resulting in: $T_p = 1.1 \cdot T_{m-10}$.

It must be noted that the two expressions for parameterizing the surface roughness are only a selection of expressions. The most appropriate definition for the surface roughness still remains a subject of debate.

Chapter 4

Area of study

4-1 Introduction

In this study, the Gemini wind farm area is used as the research site. It is located in the Dutch North Sea, some 85 kilometers north of the Dutch coast and it is size is around 68 square kilometers. The wind farm consists of 150 wind turbines, each with a rated capacity of 4 MW, giving the wind farm a total rated capacity of 600 MW. The wind farm is divided into two separate areas, called Zee-energie (ZE) and Buitengaats (BG). In both of these areas an offshore high voltage station (OHVS) is located, which is necessary for the transportation of electricity from the turbines to the land high voltage station (LHVS) in the city of Eemshaven. In the figure below, the location of Gemini and the harbour of Eemshaven can be seen.

Figure 4-1: Gemini wind farm location in the North Sea (Gemini, 2019).

Also located in the harbour of Eemshaven is the base for the service vessel of the Gemini wind farm. This service operation vessel (SOV) operates inside the Gemini wind farm area for

troubleshooting and scheduled maintenance on the present offshore wind turbines. Besides troubleshooting, maintenance is carefully planned for the long- and short term. Because service vessels can only operate under certain metocean (meteorological and ocean) conditions, their operation is highly dependent on the available weather forecasts. The SOV in this area also has certain operation restrictions, it can operate under a significant wave height of 2.5 meters.

4-2 Domain

The Gemini wind farm area lies in the Dutch North Sea, close to the German border. In Figure 4-2, the Gemini area is outlined. This particular area is used for both the atmospheric simulations as well as the spectral wave simulations. The left hand side of Figure 4-2 covers approximately the Dutch Continental Shelf, of which the domain is also used for the spectral wave model. SWAN essentially needs to perform two different simulations in order for realistic outcomes. First, a large area is simulated with a coarse resolution. The area preferred for simulation needs to be situated in the large area, because the first simulation will compute the boundary conditions for the preferred area. Second, the preferred area is simulated with a high resolution.
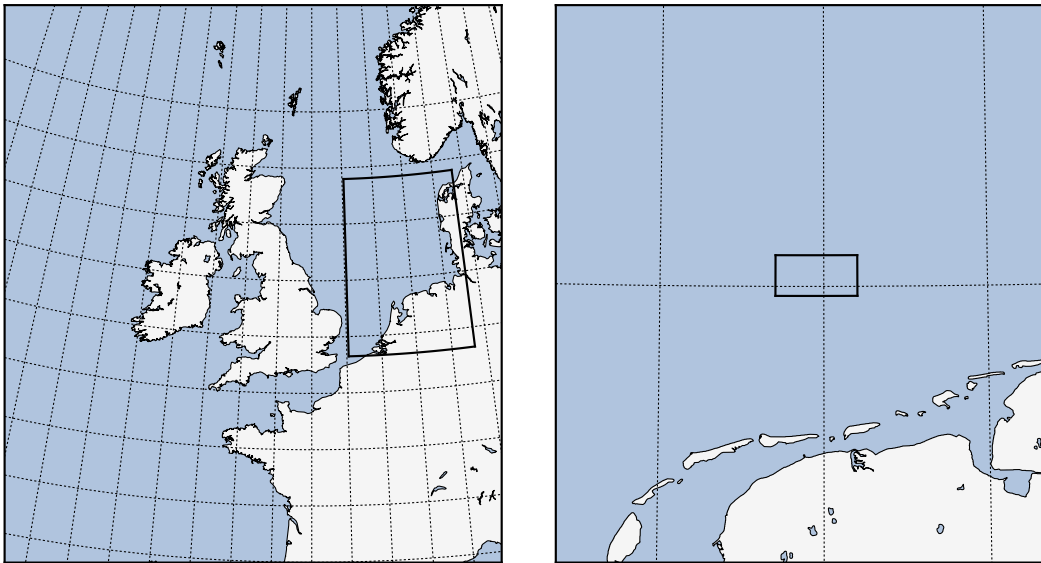
Figure 4-2: Domains of the first and second simulation for the spectral wave model.

The reason for selecting the specific area for the first simulation is because of the required input data for this simulation. At the boundaries of this area, covering approximately the Dutch Continental Shelf, specific sea state parameters must be provided as initial- and boundary conditions. Because the input data is provided by ECMWF, with their integrated ocean wave model WAM, the required parameters are therefore also consistent with oceanic waters. The strength of SWAN lies mainly in coastal waters and shelf seas. Therefore, if the boundary data provided to the SWAN domain are chosen to be at the intersection between oceanic- and shelf/coastal waters, the most realistic wave spectrum should be obtained.

Besides the oceanic and meteorological input data, also bathymetry data is required for both simulations. It was obtained via EMODnet, the European Marine Oservation and Data Network. As stated by EMODnet (2019), EMODnet was initiated by the European Commission as a service for viewing and downloading harmonised Digital Terrain Models (DTM) for the European sea regions. These are managed as survey data sets and composite DTMs by data providers from government and research. Figure 4-3 shows the obtained bathymetry for the Gemini area. Turbines are represented in black, the offshore high voltage stations are represented in red. Zee-Energie (ZE) compromises the left part of the wind farm, Buitengaats (BG) the right part.
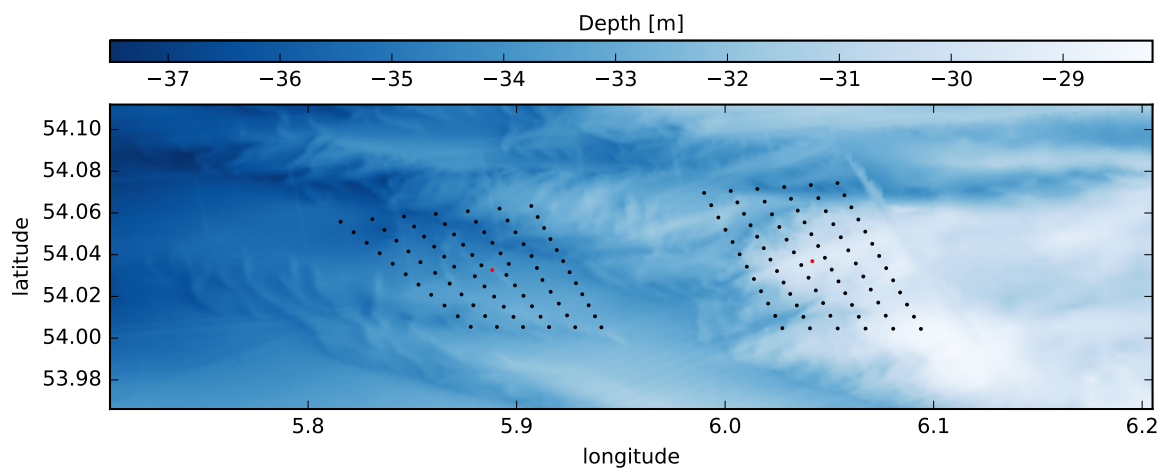
Figure 4-3: Bathymetry of the Gemini wind farm area. Also the positions of the wind turbines (black) and the offshore high voltage stations (red) are marked.

4-3 Site conditions

Before the high-resolution simulations were conducted, an analysis was performed on the metocean conditions. On both offshore high voltage stations, observation points are present to measure the atmospheric- and ocean conditions. The sea-state is measured using radio waves at a resolution of 15 minutes, the equipment is situated at 20 meters above sea level. The atmosphere is measured using a meteorological met-mast at a resolution of 10 minutes, the equipment is situated at 46 meters above sea level. For convenience, only the observations of the BG-OHVS were used in this study.

On the next page, distributions of the parameters of main concern (M, H_s) are presented, including the maximum atmospheric- and oceanic conditions for operation inside the offshore wind farm. Here, the restrictions are a wind speed of 20 m/s and/or a significant wave height of 2.5 meters. These histograms, of the full year of 2017, counted an exceeding of the maximum wind speed in 0.8% of the cases and 14.4% for the significant wave height. Therefore it can be concluded that the sea state has much more impact on offshore operations in this area.
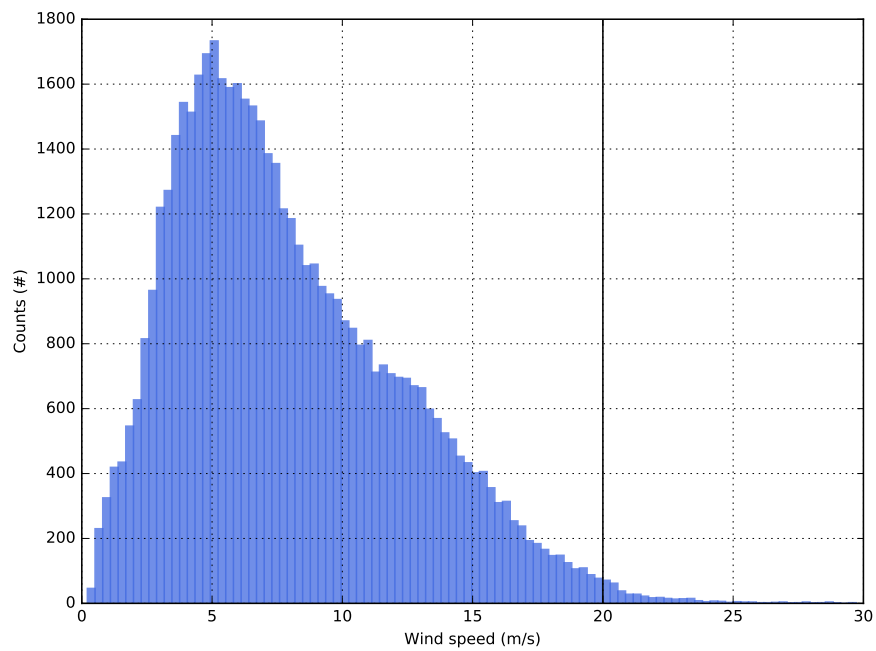
Figure 4-4: Histogram of the wind speed (M) at BG-OHVS, of the whole year 2017. The vertical line represents the maximum condition for offshore operation.
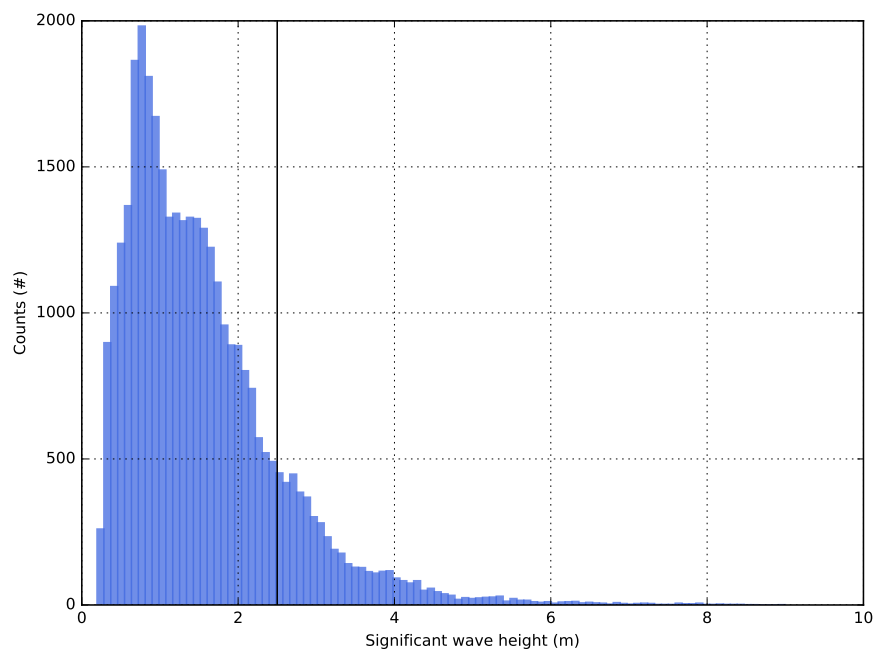
Figure 4-5: Histogram of the significant wave height (H_s) at BG-OHVS, of the whole year 2017. The vertical line represents the maximum condition for offshore operation.

Chapter 5

Method

5-1 Introduction

The atmospheric conditions were simulated by the GPU-Resident Atmospheric Simulation Platform (GRASP) and the oceanic conditions were simulated using Simulation Waves Nearshore (SWAN). In Chapter 3 and 2 both large-eddy simulations and simulations with the energy balance equation were described thoroughly in a physical way. This chapter focuses on the configurations of both simulations. Furthermore, the different data sets used for this study are discussed, including the data post-processing.

5-2 Data description

In this section, the different data sources and models used for this study are briefly discussed to provide a clear overview (see Table 5-1).

Table 5-1: Overview of data sources and models.

#	Abbreviation	Description
1.	IFS	ECMWF's operational medium-range forecast
2.	ERA5	Fifth generation of ECMWF's atmospheric reanalysis
3.	GRASP	Whiffle's operational large-eddy simulation
4.	SWAN	Third-generation spectral wave model
5.	EMODnet	European bathymetry portal
6.	Bazefield	Metocean data portal

First, the Integrated Forecasting System (IFS) is a general circulation model (GCM) that is developed and maintained by both the European Centre for Medium-Range Weather Forecasts (ECMWF) and Météo-France. In the meteorological community it considered to be the best performing operational GCM. The IFS is available in a number of different configurations. Because this study did not focused on day-ahead- or medium-range forecasting, no IFS

data was used. However, if this data was necessary for this study, the operational medium-range forecast with the integrated wave model ('HRES-WAM') should have been used.

Second, ERA5 is the fifth generation of ECMWF's atmospheric reanalysis of the global climate. The reanalysis combines IFS data with observation across the world into a consistent data set. This procedure, called data assimilation, is done every 12 hours. As stated by ECMWF (2019), a previous forecast is combined with up to date observations to assemble the best state of the atmosphere, from which an updated forecast is issued. The horizontal resolution is however reduced compared to IFS, $0.3°$ instead of $0.125°$.

Third, as already discussed in Section 3-4, GRASP is the model used for the atmospheric large-eddy simulations in this study. Each atmospheric large-eddy simulation compromises one day, including one hour spin-up and one hour spin-down time, which results in a simulation of 26 hours. The spatial grid has a horizontal resolution of 128 m and 68 vertical levels up to a height of approximately 5 km. An output is generated every 10 minutes.

Fourth, as discussed in Section 2-3-3, the SWAN model is used for the spectral wave simulations in this study. The spatial grid has a longitudinal resolution of $0.0020°$ and a latitudinal resolution of $0.0011°$. An output is generated every 10 minutes.

Fifth, EMODnet is the data source for bathymetry necessary to perform spectral wave simulations. It is obtained with a horizontal resolution of $0.00104°$. More information about this data source is provided in the previous chapter.

5-3   Atmospheric simulations

The development and physical equations of the atmospheric model used in this study was described thoroughly in Section 3-4, now the specific configurations of the simulation set-up will be discussed.

5-3-1   Domain

The area of the LES domain is approximately 33x16 km^2, with an equal grid spacing of 128 meters in the x- and y-direction. The center of the domain has the following coordinates: ($54.039°$ N, $5.955°$ E). In the z-direction, the domain starts at the ocean surface and each grid spacing increases the higher the model level n. The bottom grid cells have a height of $\Delta z_0 = 40$ m, and each model level increases with a factor of $\alpha = 1.787\%$.

$$\Delta z_n = \Delta z_0 (1 + \alpha)^n \tag{5-1}$$

The highest model level has a grid spacing of around $\Delta z_{67} = 129$ m, which ends the domain at a height of around 5 km.

5-3-2   Initialization

As discussed in Section 5-2, each simulation covers one day. For this study, a simulation was performed of every day in January and February 2017. The reason for selecting these months is twofold. First, the available observations were complete for the whole year of 2017.

Second, simulating two months in total was chosen to reduce computation time of all the performed simulations. The simulations were initialized by ERA5, which means that they are hindcasts. Initialization starts at 23:00 UTC on the day before the day of interest and stops at 01:00 UTC the day after, totalling the simulation time at 26 hours. The required initial conditions u, v, q_t, θ_l are obtained from ERA5 by the parameters, $u^E, v^E, T^E, p^E, q_v^E, q_l^E, q_i^E$. To match the required parameters to the GRASP grid, the parameters from ERA5 are linearly interpolated and converted into the GRASP prognostic variables using the following relations (van Laarhoven, 2019):

$$u = u^E \tag{5-2}$$

$$v = v^E \tag{5-3}$$

$$q_t = q_v^E + q_l^E + q_i^E \tag{5-4}$$

$$\theta_l = \frac{T^E}{\Pi} - \frac{L_{heat}}{c_{pd}\Pi} q_c \tag{5-5}$$

Here u and v are the horizontal wind velocity components, q_t is the (non-precipitating) water specific humidity, q_v is the water vapor specific humidity, q_l the liquid water specific humidity, q_i the ice specific humidity, θ_l is the liquid water potential temperature, T is the temperature, L_{heat} is the latent heat release upon vaporization, c_{pd} is the specific heat capacity of dry air, q_c the cloud specific humidity and Π is given by:

$$\Pi = \left(\frac{p^E}{p_{ref}}\right)^{R_d/c_{pd}} \tag{5-6}$$

where p and p_{ref} are the pressure and reference pressure, R_d is specific gas constant of dry air.

5-3-3 Boundary conditions

In this section the lower-, horizontal- and upper boundary conditions of the atmospheric simulations are discussed. The lower boundary conditions were essentially discussed in Section 3-4-2. However, this changes for the two-way coupled simulations.
GRASP uses periodic boundary conditions in the horizontal direction, meaning that the outflow at the downstream side of the domain is fed into the inflow of the upstream side of the domain. However, this becomes problematic if obstacles like wind turbines are implemented into the simulation. The wake behind the obstacle would then be fed into the inflow, which causes unrealistic results. A solution for this is to perform simulations with the concurrent cursor-precursor method, based on Stevens et al. (2014) and Munters et al. (2016). Simultaneously, a precursor- and cursor simulation is performed. The precursor simulation has an obstacle free domain which runs on the same domain size and resolution as the cursor simulation, flow in this simulation is considered as free stream. The cursor is the simulation of interest which include obstacles like wind turbines. At the edges of this cursor domain, the

prognostic variables are nudged towards the values of the precursor simulation which allows the use of periodic boundary conditions (Figure 5-1). This solution is found back as an extra term in the governing equations (Equation 3-24 and 3-27):

$$F_i^{nudge} = -\frac{a(x,y,z)\eta}{\Delta t}(\chi_i^1 - \chi_i^0) \qquad (5\text{-}7)$$

Here, $a(x,y,z)$ is a spatial function, η is the nudge factor, Δt is the time step, χ_i^1 is the prognostic variable in the cursor and χ_i^0 in the precursor. The spatial function is 0 at the start of the nudging zone and increases to a value of 1 to the edge of the domain. In the simulations performed, η was set to 0.3 and Δt is the simulation time step (Bon, 2019).
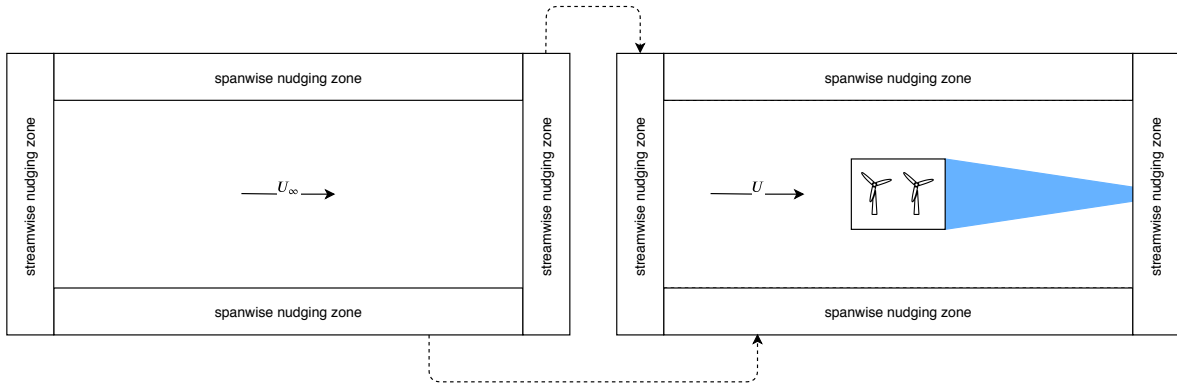
Figure 5-1: The precursor and cursor domains, adapted from Bon (2019).

At the top of the domain, the boundary conditions for the prognostic variables are relatively straightforward Heus et al. (2010):

$$\frac{\partial \widetilde{u}}{\partial z} = \frac{\partial \widetilde{v}}{\partial z} = 0, \qquad \widetilde{w} = 0, \qquad \frac{\partial \widetilde{\phi}}{\partial z} = \text{constant} \qquad (5\text{-}8)$$

5-3-4 Large-scale forcing

Atmospheric large-eddy simulations, like GRASP, need to apply large-scale forcings to account for large-scale atmospheric effects. These effects are large-scale pressure gradients and the Coriolis force, which results in large-scale horizontal- and vertical advective transport and the geostrophic wind. Data from a general circulation model was therefore again needed to account for these effects, which was provided again by ERA5.

5-4 Wave simulations

The development and physical equations of the spectral wave model used in this study was described thoroughly in Chapter 2, now the specific configurations of the simulation set-up will be discussed. Simulation of the large domain was always performed with ERA5 wind fields. The simulations of the smaller domain of interest were performed with three different wind fields; a simulation forced by ERA5 wind fields, a simulation forced by GRASP wind fields without turbines and a simulation by GRASP wind fields with turbines.

5-4-1   Domain

As already discussed in Section 4-2, two simulations were performed on two different domains. The large domain was discretized into 163 x 199 grid points, which results in a resolution of 0.05° x 0.033°. The spectral domain had a directional coverage of 360°, discretized into 45 directions. The frequency range was set from 0.03 to 2.5 Hz, to account for high frequency young waves. The small domain was discretized into 256 x 128 grid points, which results in a resolution of 0.0020° x 0.0011°. This is an equal grid resolution as the atmospheric simulations. The spectral domain and frequency range were set equal to the simulation of the large domain.

5-4-2   Initial and boundary conditions

On the larger domain, input parameters obtained from ERA5 were provided at the boundaries. Following the boundary at sea, input was provided at a resolution of 0.3° every hour, smaller time steps were linearly interpolated by SWAN. The required input wave parameters consist of the significant wave height (H_s), the peak wave period (T_p), the mean wave direction (θ_{wave}) and the power of the directional spreading (m). The power of the directional spreading is obtained via Equation 2-10, where the spectral directional width is obtained via ERA5. These parameters are subsequently used to construct a generalized frequency wave spectrum, a JONSWAP spectrum, with a $\cos^m \theta$ directional distribution (Equation 2-8). The JONSWAP spectrum is given by the following form (Journée and Massie, 2001):

$$E(f) = \frac{320H_s^2}{T_p^4}f^{-5}\exp\left\{\frac{-1950}{T_p^4}f^{-4}\right\}\gamma^{\exp\left\{-\left(\frac{\frac{T}{T_p}-1}{\sigma\sqrt{2}}\right)^2\right\}} \tag{5-9}$$

where γ is a peak enhancement parameter and is equal to 3.3. Furthermore, σ is equal to 0.07 if $f < f_p$ and equal to 0.09 if $f > f_p$. The JONSWAP spectrum is used in this study to construct the boundary conditions, more information about generalized wave spectra can be found in Holthuijsen (2007). By using a generalized wave spectrum at the boundaries, the simulations require some spin-up time to provide realistic spectra. In this study, a spin-up of ten timestamps (100 minutes) was used for all simulations.

5-4-3   Wind field

Wave generation by wind is the most driving factor in wave growth. As discussed in the beginning of this section, simulations were performed with three different wind fields. The ERA5 wind field has a resolution of 0.3° x 0.3°, the GRASP wind fields have a resolution of approximately 0.002° x 0.001°.
SWAN requires the wind field to be provided by the wind velocity components at 10 meter height. Subsequently, it converts the 10 meter wind speed U_{10} into the friction velocity u_* by the relation of Wu (1982):

$$u_*^2 = C_D U_{10}^2, \qquad C_D = \begin{cases} 1.2875 \times 10^{-3}, & \text{for } U_{10} < 7.5\text{m/s} \\ (0.8 + 0.065U_{10}) \times 10^{-3}, & \text{for } U_{10} \geq 7.5\text{m/s} \end{cases} \tag{5-10}$$

However, this relation does not account for atmospheric stability and the atmospheric simulation directly solves the friction velocity. So, it is preferred to use the friction velocity u_* computed by GRASP, but SWAN does not allow a direct forcing by u_*. Therefore, the friction velocities from GRASP are converted into *'pseudo wind speeds'* by using the inverse of the Wu (1982) relation. Providing these *'pseudo wind speeds'* to SWAN, will make sure that SWAN uses the friction velocity computed by GRASP.

5-4-4   Model physics

SWAN contains a number of physical processes, which are provided by physical parameterizations, that add or withdraw wave energy to or from the wave spectrum. Most processes were set in the default setting, except for bottom friction dissipation which is given by the JONSWAP formulation of Hasselmann et al. (1973) and depth-induced wave breaking which uses a constant breaker index. More information can be found in SWAN (2019).

5-5   Coupled simulations

The physical connection between large-eddy simulations and spectral wave modelling was already discussed in Section 3-5, now the specific configurations of the simulation set-up will be described.

5-5-1   One-way coupling

The simulations which uses ERA5 wind fields for the large domain and GRASP wind fields for the small domain are here abbreviated with one-way coupled simulations. However, both ERA5 data and GRASP data need to be processed in order to provide these wind fields to SWAN. For ERA5 data it was relatively straightforward. Because data from ERA5 can only be obtained in a resolution of one hour, SWAN linearly interpolates this data for smaller time steps. Providing GRASP data to SWAN proved to be not so straightforward. In the first place because a GRASP simulation is on a rectangular grid, a SWAN simulation is on a spherical grid. Therefore the GRASP grid needs to be slightly modified in order to fit on the SWAN grid. Because the GRASP domain is defined by its centre geographical coordinates, the boundaries of the domain can be converted also in geographical coordinates instead of a distance from the origin. Once this step is undertaken, it is possible to provide SWAN with GRASP wind fields in geographical coordinates.

Second, GRASP is requested to write its values every 10 minutes to the output file. However, these values are not written exactly at 10 minutes, so these values need to be linearly interpolated in time. This is because GRASP needs to follow the Courant criterion for its simulation time steps. Third, the two grids of GRASP and SWAN need to be shifted. This is because the full levels of GRASP, which are essentially the centres of the grids, need to be aligned with the origins of the SWAN meshes. This is illustrated in the right part of Figure 5-4. After these steps are finalized, the produced netCDF file can be provided to SWAN to perform a one-way coupled simulation (Figure 5-2).
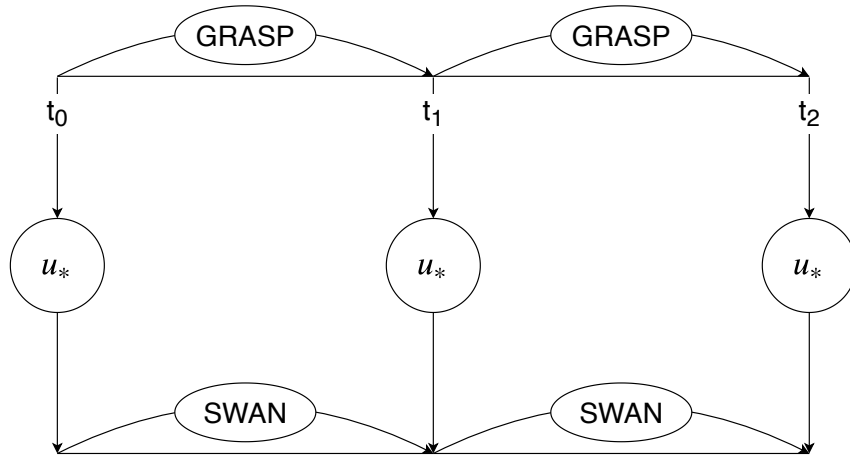
Figure 5-2: Schematic overview of one-way coupled system.

5-5-2   Two-way coupling

As can be seen in Figure 3-3, a momentum exchange between GRASP and SWAN is necessary in order to run a two-way coupled simulation. To do so, the values of u_* and z_0 have to be exchanged every time step between the two models.

The interface called ASPIRE (Atmospheric Simulation Platform for Innovation Research Education) allows this exchange of variables in GRASP with other numerical models. In this research, the atmospheric model and the spectral wave model are interacting with each other every coupling time step. As stated by Janssen et al. (2002), the atmospheric model is run for a coupling time step, then the spectral wave model is called by the atmospheric model, forced with a wind field of the atmospheric model, after which the atmospheric model is run for the next coupling time step, now using the roughness length (z_0) as determined by the spectral wave model during the previous interaction period. Figure 5-3 provides a schematic representation of the steps described above.
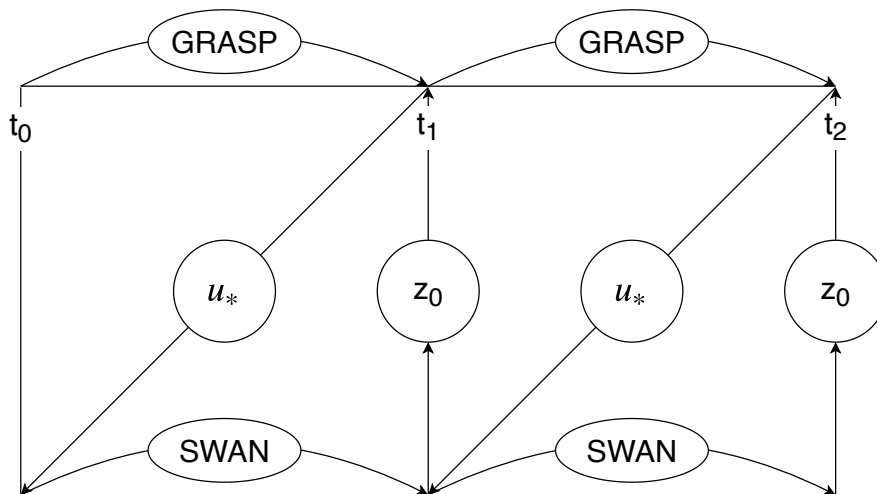
Figure 5-3: Schematic overview of two-way coupled system, modified from Janssen et al. (2002).

As mentioned in Section 5-2, a GRASP simulation needs to be performed per day. Therefore, two-way coupled simulations have to run in the same configuration. In order to do so, the wave field from the last time step of the particular day needs to be saved in order that it can be used as an initial condition again for the new day. This is solved in SWAN by using 'hotstart' files, were the initial wave field from the previous SWAN run is saved.

Furthermore, as already described in the previous section, the centers of the grids of GRASP need to be aligned with the mesh points of SWAN. This is because the full levels of GRASP, need to perform the momentum exchange with the origins of the SWAN mesh (right part of Figure 5-4).
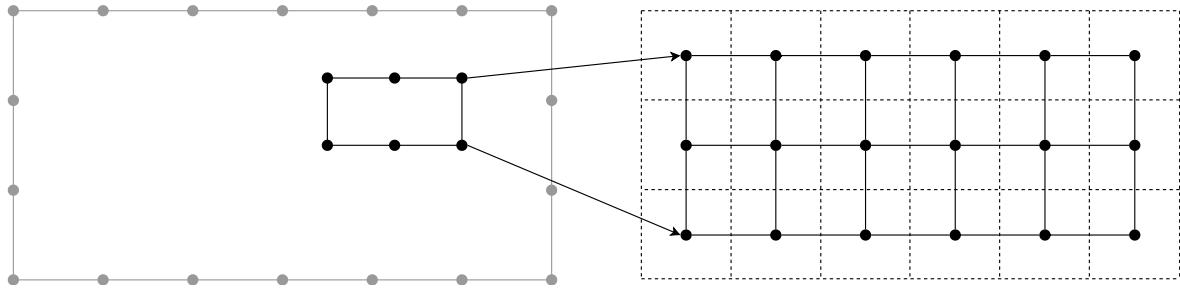
Figure 5-4: Left: large domain (indicated with grey) forced by ERA5 wind field. Right: area of interest (indicated with black) forced by GRASP wind field. Here, the GRASP grid is indicated by the dashed lines. The dots indicate the concerned boundary conditions or grid points.

To summarize, a two-way coupled simulation is performed according to the following steps. First, a (uncoupled) SWAN simulation is performed on a large domain with a coarse resolution. The boundaries of the wave spectrum are provided by a JONSWAP spectrum obtained via ERA5 parameters, the wind field on the large domain is also provided by ERA5. Once this simulation is finalized, the boundaries of the area of interest in the large domain are saved in a nest file. Second, a two-way coupled simulation is performed of the area of interest on a high resolution. The boundaries of the wave spectrum are provided by the nest file computed in the simulation of the large domain, the wind field is provided by GRASP and at every time step a momentum exchange (u_* and z_0) is performed between the atmospheric model and the spectral wave model. Figure 5-4 illustrates the steps described here.

As mentioned in Section 5-3-3, a GRASP simulation is executed by using the concurrent cursor-precursor method. In a two-way coupled GRASP-SWAN simulation this method is also necessary. However, a two-way coupled precursor simulation still needs to operate in a one-way coupled configuration.

Figures 5-5 and 5-6 show the flowcharts of both coupling configurations to provide a clear picture of the simulations. The dashed block in the flowcharts indicates the part of all simulation steps were the actual momentum exchange takes place.

Figure 5-5: Schematic overview of one-way coupled simulation. Here, the grey blocks indicate the input data, the blue blocks represent the atmospheric simulations and the yellow blocks indicate the wave simulations. Initial conditions are denoted by I.C., boundary conditions by B.C., large-scale forcing by forcing and oceanic depth by d. The one-way coupled configuration is enclosed by the dotted rectangle.

Figure 5-6: Schematic overview of two-way coupled simulation. Here, the grey blocks indicate the input data, the blue blocks represent the atmospheric simulations and the yellow blocks indicate the wave simulations. Initial conditions are denoted by I.C., boundary conditions by B.C., large-scale forcing by forcing and oceanic depth by d. The two-way coupled configuration is enclosed by the dotted rectangle.

5-6   Overview of simulations

Various simulations with GRASP and SWAN were performed, in a uncoupled-, one-way coupled- and two-way coupled configuration. Several simulation cases were devised, which are summarized in Table 5-2 below.

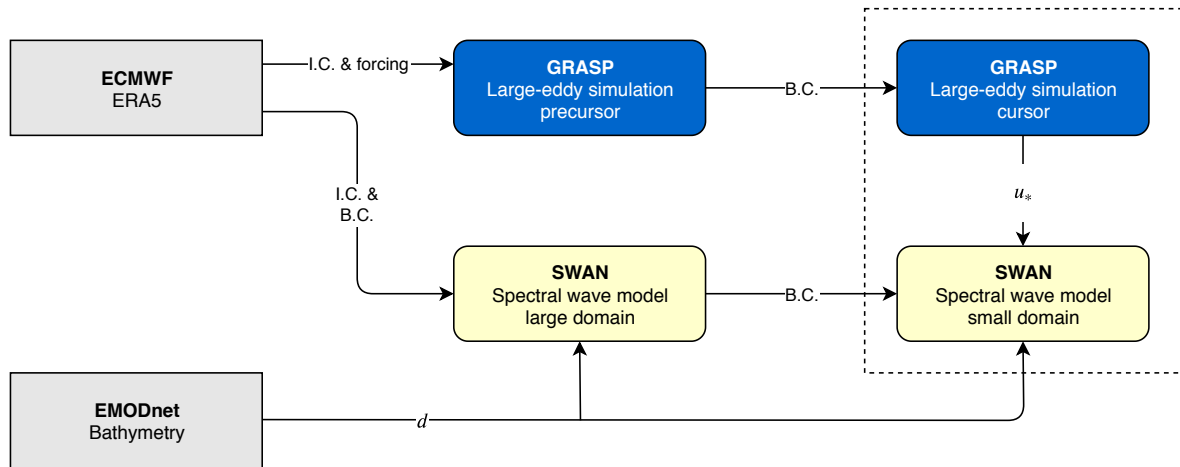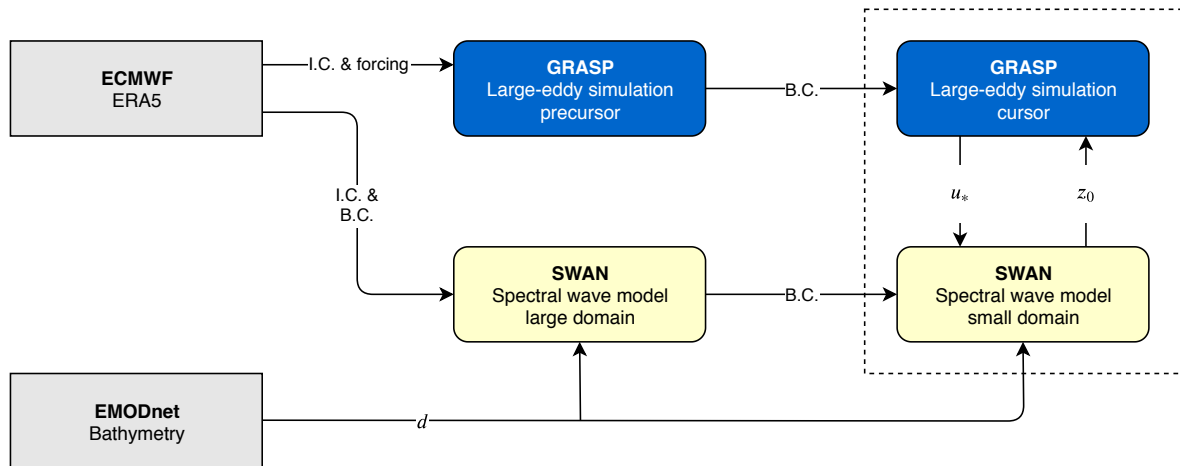**Table 5-2:** Simulations overview. Here, the atmospheric simulations are denoted by LES (large-eddy simulation) and the wave simulations are denoted by SWS (spectral wave simulations).

Abbreviation	Description	Model	Input
A	LES without turbines	GRASP	ERA5
B	LES with turbines	GRASP	ERA5
1C-E	SWS of wind farm	SWAN	ERA5
1C-A	SWS of wind farm	SWAN	GRASP-A
1C-B	SWS of wind farm	SWAN	GRASP-B
2C-A	LES/SWS of wind farm	GRASP-A/SWAN	ERA5
2C-B	LES/SWS of wind farm	GRASP-B/SWAN	ERA5

Simulation A, the GRASP precursor simulation (without turbines) of the wind farm area, was performed for the identification of heterogenic effects in the following simulation. Simulation B, the GRASP cursor simulation (with turbines) of the wind farm area, was performed to act has the high resolution turbulence-resolving simulation of the wind farm area. Both simulation A and B simulated the entire year of 2017, on a 10 minute time resolution. However, because of the computational costs, only the months January and February of this year were eventually used for the following simulations.

For simulation 1C-E, the first SWAN simulation, ERA5 input data was used to provide a benchmark for the subsequent spectral wave simulations with higher resolution wind forcing. Simulation 1C-A consisted of providing the small domain with wind fields from GRASP-A, the large-eddy simulation without turbines. Boundary conditions and wind fields for the simulation of the larger domain were obtained from ERA5. Subsequently, simulation 1C-B, compromises the forcing of the small domain with GRASP-B wind fields, the simulation including turbines.

Furthermore, simulation 2C-A is in essence performed in the same configuration as simulation 1C-E. However, a momentum exchange is now included, which results in executing a two-way coupled simulation. Simulation 2C-B runs in the same configuration as simulation 1C-B, only this simulation is now two-way coupled.

Using the described simulations, key results were identified concerning hindcast performance, modelling of the sea state and interaction between the numerical models through the roughness length. The next chapter will provide a comprehensive insight in the obtained results.

Chapter 6

Results and Discussion

6-1 Introduction

In the previous chapters, the atmospheric large-eddy simulation and spectral wave model were treated in a physical way and their simulation set-up was presented, both in an one-way- and two-way coupled configuration. This chapter provides the results obtained from the simulation cases. The results are discussed and analyzed in detail to provide insights into the heterogenic effects on the wave spectrum, roughness length parameterizations and hindcast performance.

6-2 Heterogenic effects on wave spectrum

This section addresses the effects of forcing the spectral wave simulations with the turbulence-resolving atmospheric simulation performed by an atmospheric large-eddy simulation. By looking at Figure 6-1 on the next page, it can be identified that the atmospheric parameters, the horizontal wind magnitude (M), the wind direction (θ_{wind}), the wind in the longitudinal direction (u) and the wind in the latitudinal direction (v), have an influence on the oceanic conditions. The wind turbines do not only have an impact on the wind speeds downstream, also the wind direction is influenced by the increased amount of turbulence in the wake region. This directly impacts the frequency-direction wave spectrum, causing a reduction in significant wave height and an altering in wave direction in the wind farm area. The peak period (T_{ps}) is not influenced by the wind farm, because it does not contain the wave period of young waves. Because the wind wake causes a reduced amount of higher frequency waves (capillary waves), the mean wave period in the wake region is increased. If then more weight is given to lower frequency waves in computing the mean wave period (T_{m-10}), an increased mean wave period can be identified in the wake region. Note that in this section, the horizontal wind magnitude (M), the wind in the longitudinal direction (u) and the wind in the latitudinal direction (v) are obtained using the inverse relation of Wu (1982). This transforms the friction velocities (u_*) into 10 meter (pseudo) wind velocities (see Section 5-4-3).
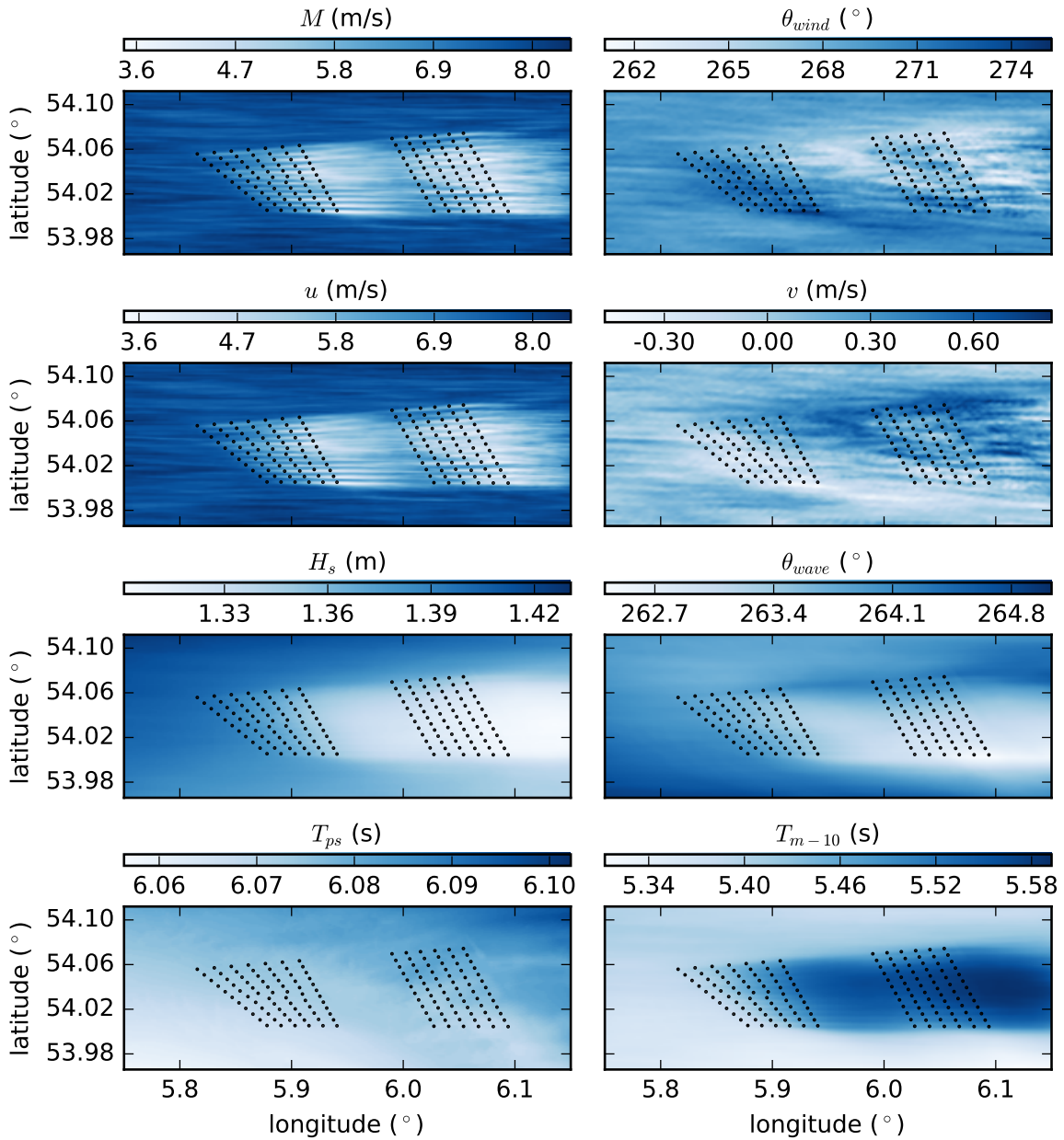
Figure 6-1: Contour plots of the effects of wind turbines on a number of atmospheric- and ocean conditions. All contours are from the same moment in time: 2017, February 19, 10:30 UTC. The contour plots were obtained from simulation 1C-B, the one-way coupled GRASP/SWAN configuration.

These contour plots are however just a snapshot of the atmospheric- and oceanic conditions at a particular time. If the evaluated amount of time stamps were to be increased, a better picture should arise under which conditions these heterogenic effects occur. Therefore, for all pixels in the domain, the significant wave height is obtained, at every time stamp of the simulation. To assess whether the distributions of the other simulations (1C-E, 1C-A, 2C-A, 2C-B) are different, they are also included in Figure 6-2.
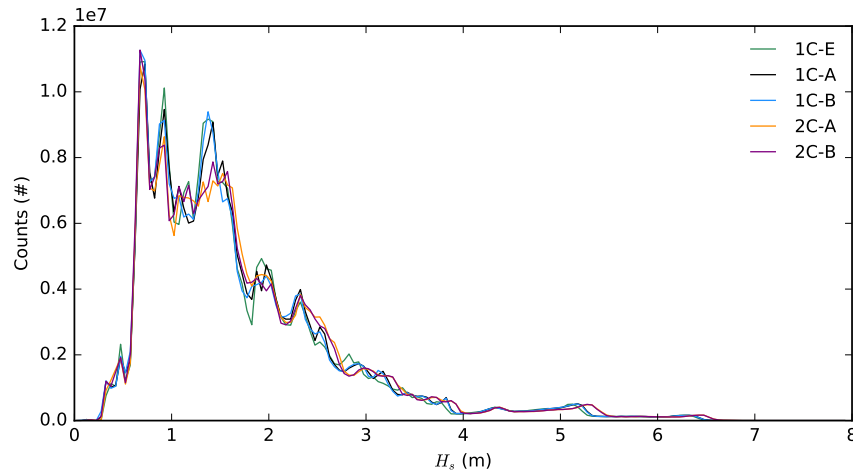
Figure 6-2: Distribution of H_s, everywhere in the domain, for the different performed simulations.

Figure 6-2 shows that in general, the different distributions are matched quite evenly. But, around a H_s of 1.5 meter, a decrease in counts for the two-way coupled simulations is observed. This might indicate a region were a substantial amount of momentum exchange takes place between the atmosphere and waves. In the next section, this is discussed further.

6-2-1   Conditions of occurrence

To identify whether a decrease in the significant wave height caused by heterogenic effects occurs, the ideal conditions for these wave wakes need to be studied. Therefore the following parameter is considered, the spatially averaged decrease of H_s over the entire domain between the simulation with- and without turbines;

$$\Delta\overline{H}_s(t) = \overline{H}_{s,A}(t) - \overline{H}_{s,B}(t) \tag{6-1}$$

The parameter $\Delta\overline{H}_s$ is used to identify the possible occurrence of a wave deficit under certain atmospheric- and oceanic conditions. Furthermore, $\Delta\overline{H}_{s,A}$ denotes the spatially averaged H_s in the simulation without turbines and $\overline{H}_{s,B}$ represents the spatially averaged H_s in the simulation with turbines. Figures 6-3 and 6-4, presented on the next page, will elaborate further on these conditions. Note that in this section, the one-way coupled GRASP/SWAN simulation is analyzed (simulation 1C-B).
In Figure 6-3, relevant atmospheric- and oceanic parameters (M, θ_{wind}, θ_{wave}, ζ) are scattered in relation to the significant wave height. It can be deduced that H_s follows exponential growth if the horizontal (pseudo) wind magnitude at 10 meter is increased. Furthermore, large values for the significant wave height are identified in neutral stability conditions ($\zeta = 0$). The other two parameters (θ_{wind}, θ_{wave}) show a spread scatter.
In Figure 6-4, the chosen atmospheric- and oceanic parameters which could force a wave deficit are scattered as a function of the wave height deficit ($\Delta\overline{H}_s$). The parameters θ_{wind} and θ_{wave} look rather uncorrelated with the wave deficit. However, the fit trough the scatter of the pseudo wind magnitude matches the shape of a typical thrust curve of a wind turbine.

Indicating that the wind turbine acts as a withdrawing force on the wind speed which has a direct impact on the wave spectrum below. The magnitude of this withdrawing force and the consequent deficit in the process of wave generation by wind therefore follows the shape of the thrust curve. Also, the significant wave height deficit is the largest in neutral stability conditions.
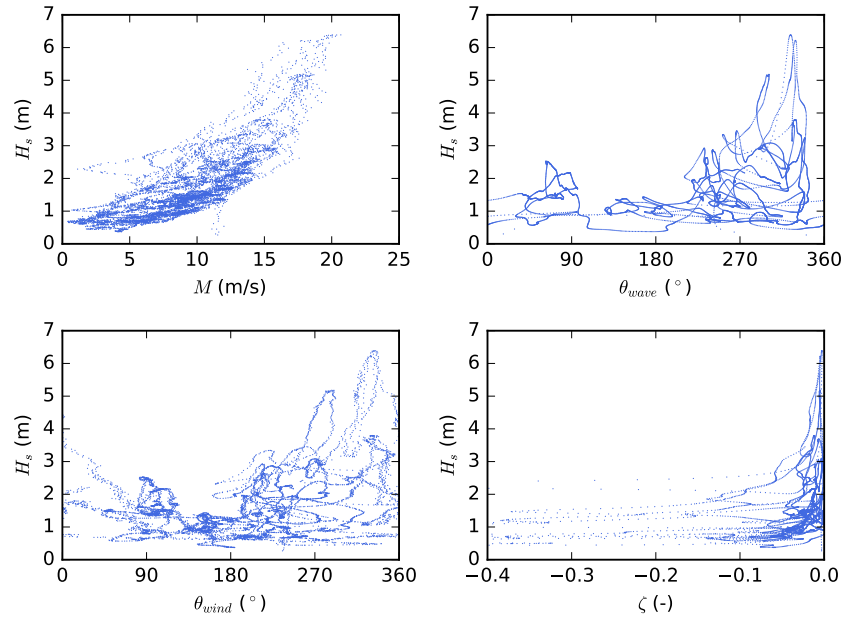
Figure 6-3: Conditioning of the significant wave height (H_s) with the chosen parameters.
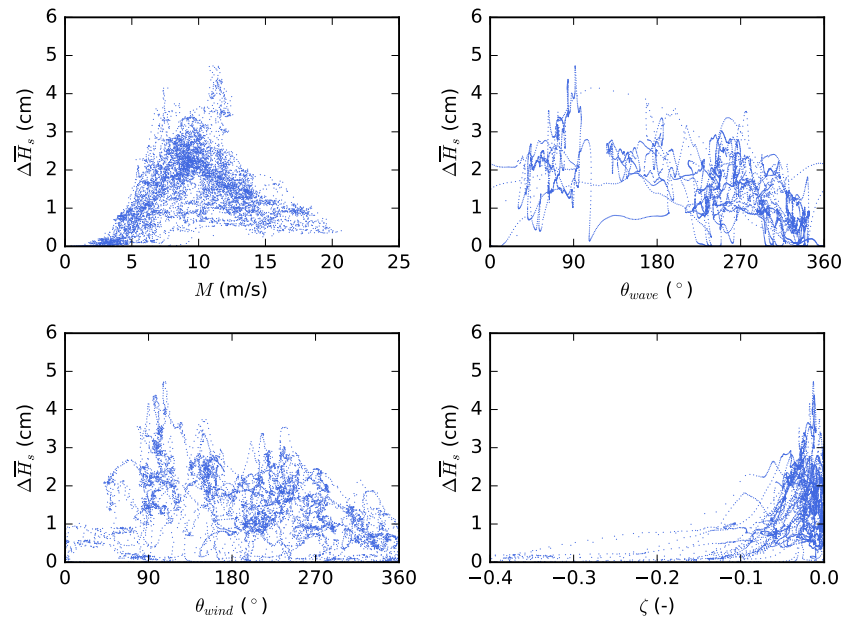
Figure 6-4: Conditioning of the significant wave height deficit $(\Delta \overline{H}_s)$ with the chosen parameters.

Subsequently, Figure 6-5 shows the chosen parameters scattered with the associated other parameters. The magnitude of a wave deficit in the simulation is indicated by the colored points. Additional information that can be deduced from these scatter plots is that the predominant wind- and wave direction, favourable for a wave deficit, is coming from the east in the performed simulation. A further analysis shows that from this direction wind speeds corresponding to the top of the thrust curve are most common in this simulation. Also, when the wind- and wave direction are aligned, favourable conditions arise for a decrease in significant wave height, which is in agreement with Equations 2-22 and 2-24.
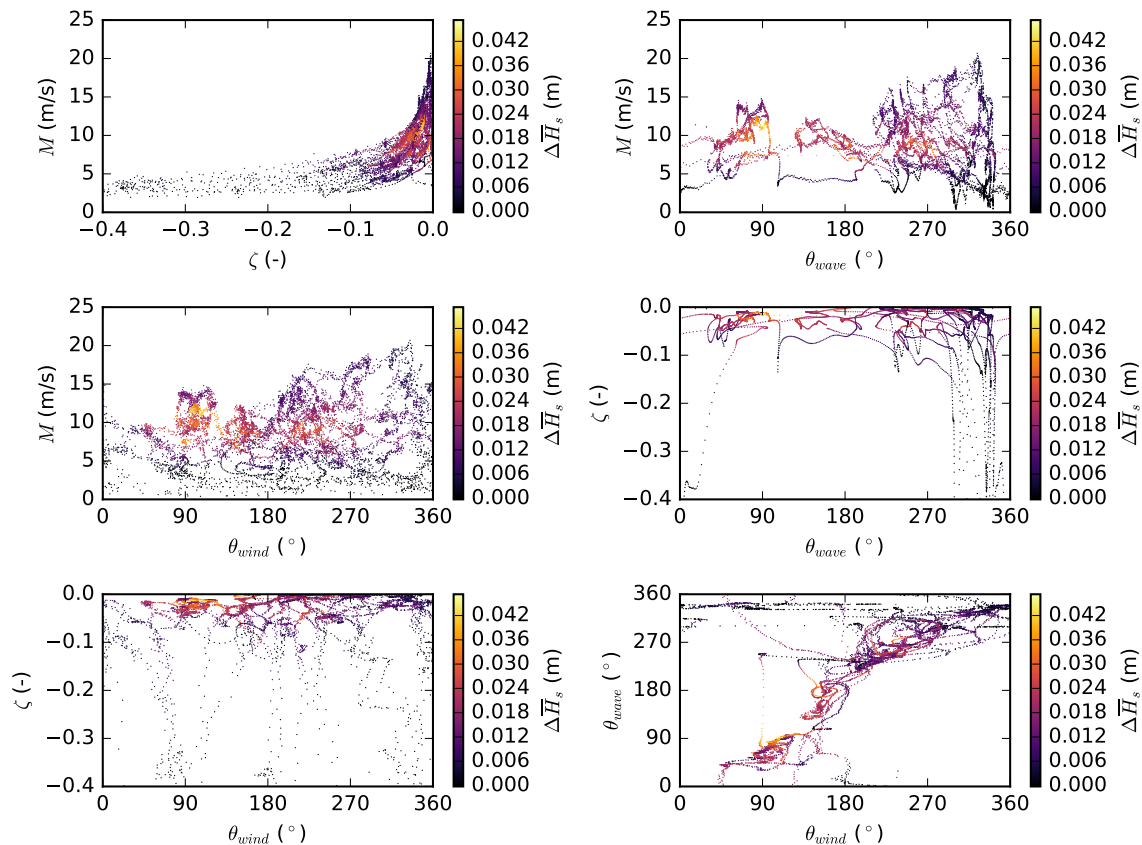
Figure 6-5: Conditions for the occurrence of a decrease in average significant wave height by heterogenic effects.

It can be deduced from Figure 6-6, on the next page, that the most predominate wind directions in the performed simulation period are from the east- and southwest direction. However, the conditioning of Figure 6-5 is somewhat limiting concerning the wind directions, mainly because of the simulation period of two months. Therefore, Figure 6-7 shows the average significant wave height deficit corresponding to each wind velocity interval, now only the predominate wind direction in the performed simulation is considered. It can be identified that for lower wind speeds (0-2 m/s), no deficit is identified. At moderate wind speeds (6-12 m/s) an average significant wave height deficit is observed in the wind wake region. In the wind speed regions of 2-6 m/s and 14-18 m/s, heterogenic effects have less impact on the wave field.
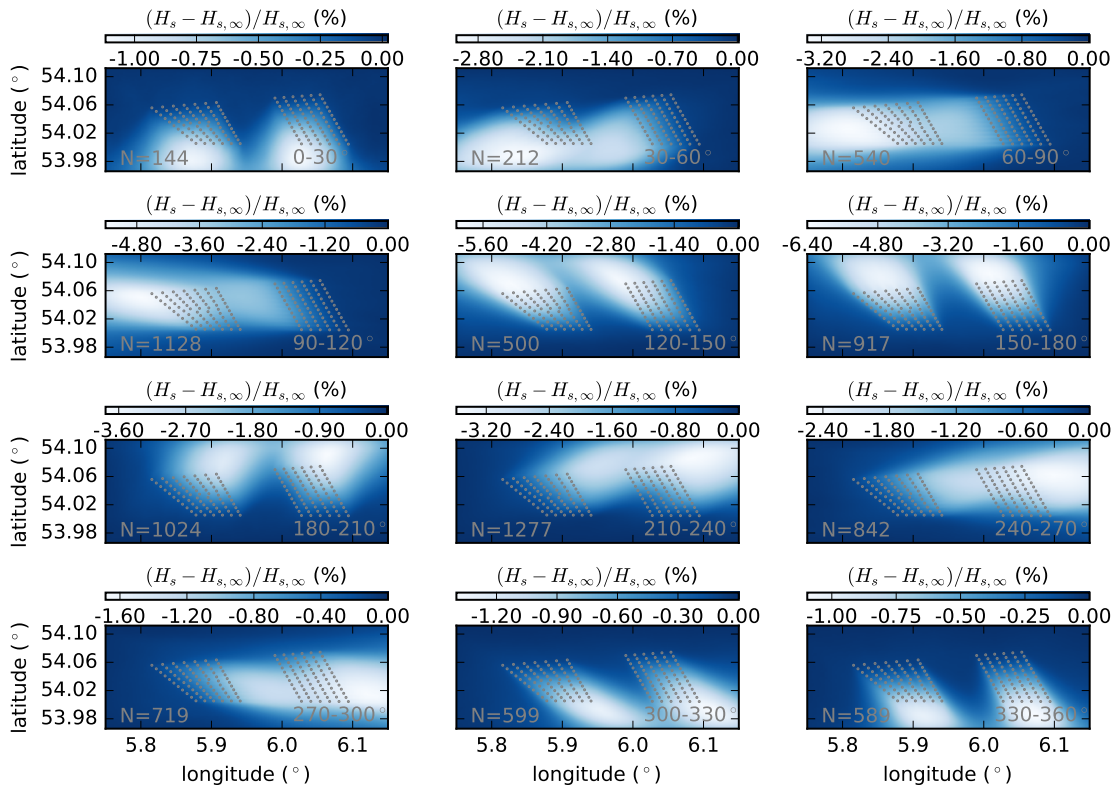
Figure 6-6: Average significant wave height deficit for each wind direction interval.
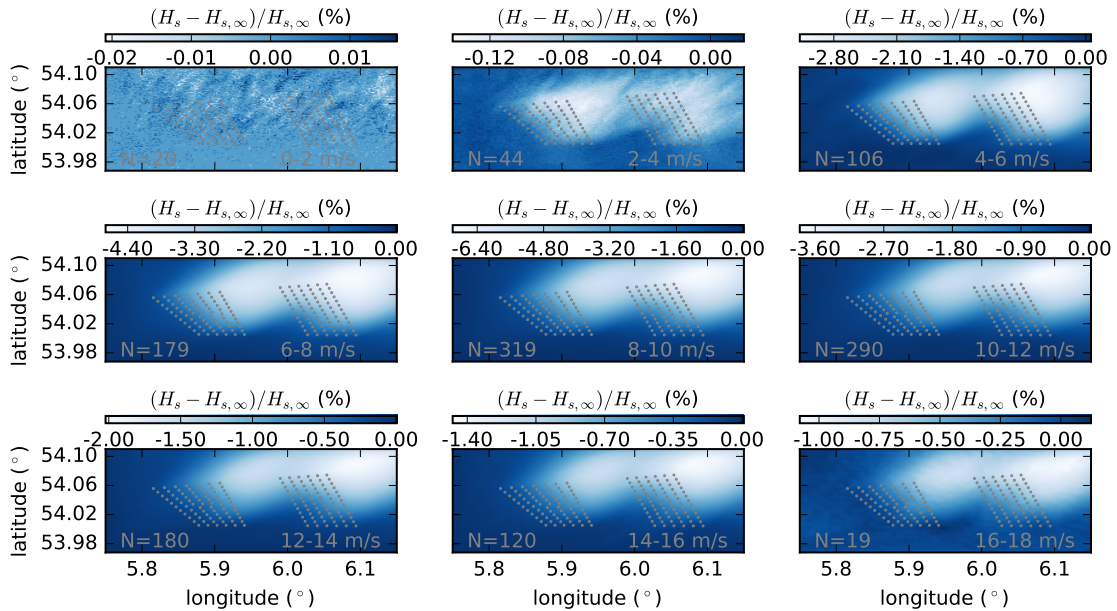
Figure 6-7: Average significant wave height deficit for each wind speed interval, considering wind from the southwest direction (210-240°).

6-2-2   Effect of two-way coupling

The above conditioning of the significant wave height deficits were performed using simulation 1C-B, the one-way coupled GRASP/SWAN simulation. To identify if these conditions are also valid for the two-way coupled simulation, a similar analysis was performed on simulation 2C-B. The analysis showed similar results concerning the occurrence of significant wave height deficits, these results were therefore reported in Appendix A.

In order to provide a qualitative comparison between the 1C-A, 1C-B, 2C-A and 2C-B simulations, a cross section of the averaged friction velocity- and wave fields for the different simulations in the longitudinal direction is obtained (Figure 6-8).
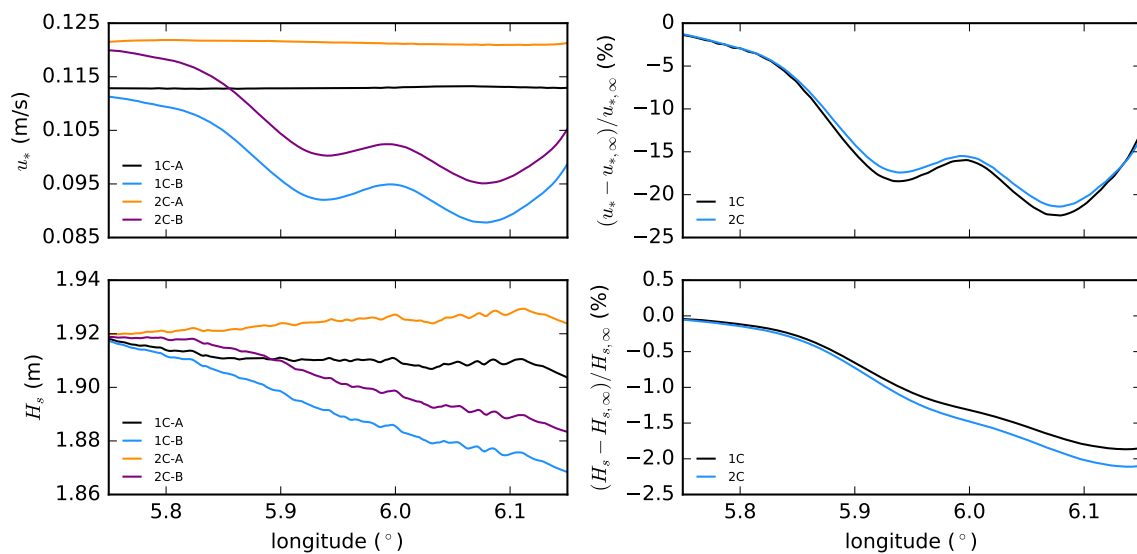
Figure 6-8: Friction velocity- and significant wave height deficits for the one- and two-way coupled simulation. Here, the graphs on the left hand side were constructed considering a wind direction from the west and wind velocities between 6-12 m/s. The graphs on the right hand side present the corresponding friction velocity- and significant wave height reduction with respect to the free stream values.

Figure 6-8 shows the averaged cross sections of the streamwise friction velocity- and wave fields in the domain, for the one-way- and two-way coupled simulations. Furthermore, the horizontal friction velocity- and significant wave height deficits with respect to the free stream are presented for the one-way- and two-way coupled simulations. Increased values for the horizontal friction velocities and wave conditions in the two-way coupled configuration originate from the momentum exchange between the atmospheric- and spectral wave model. On average, the friction velocities are higher in the two-way coupled configurations, indicating that the relation of Taylor and Yelland (2001) provides a higher value for the roughness length in comparison to the relation of Charnock (1955) in the same atmospheric conditions, causing an increased drag coefficient in the two-way coupled simulation. Subsequently, the larger friction velocities cause more wave growth. Hence, the increased values for the significant wave height in the two-way coupled configuration.

Now that the significant wave height deficits have been identified for both coupling configurations, a further analysis was performed on the average decrease in significant wave height

in the wind farm lot with respect to the wind velocity.
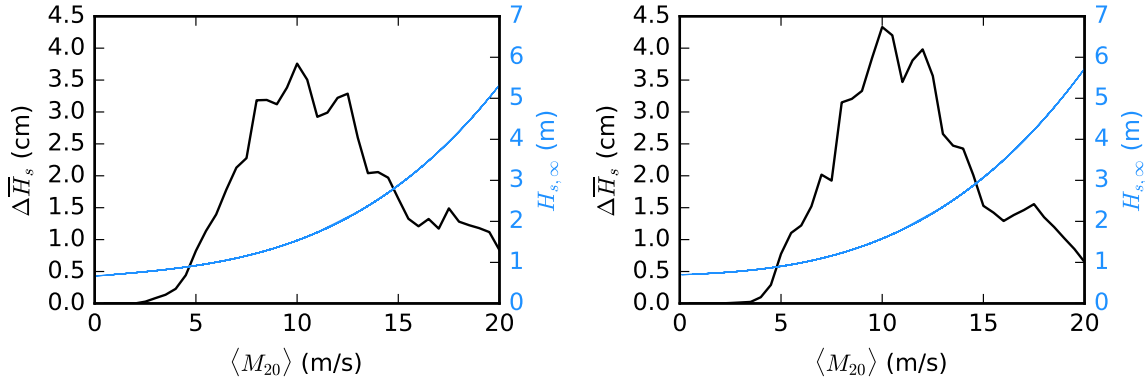
Figure 6-9: Significant wave height deficits and wave growth as a function of the slab averaged wind velocity magnitude at an altitude of 20 meters. The graph on the left represents the one-way coupled simulation, the graph on the right represents the two-way coupled simulation.

Figure 6-9 shows that the spatially averaged significant wave height deficit follows the same pattern as in Figure 6-4, for both the one-way- and the two-way coupled configuration. The wave growth of the one-way- and two-way coupled is comparable. Moreover, the two-way coupled configuration has a larger peak value for the spatially averaged significant wave height deficit compared to the one-way coupled simulation. This is also identified in Figure 6-8, where the significant wave height deficit is increased for the two-way coupled simulation due to an increased average friction velocity in both two-way coupled simulations.

6-3   Effect on roughness length

In the previous section, heterogenic effects on the friction velocity- and wave fields were analyzed for the one-way and two-way coupled simulations. This showed an offset in the friction velocity- and wave fields, indicating a reduced value for the roughness length, and therefore reduced drag, in the one-way coupled simulation.

This section presents the results of these differences in roughness lengths, as discussed in Section 3-5, and its alteration in offshore wind farm conditions. The roughness length is an important parameter in the atmospheric boundary layer because it characterizes the amount of momentum exchange with the surface. Therefore, not only an atmospheric model is directly impacted by a more realistic representation of the roughness length, also subsequent processes dependent on atmospheric conditions could benefit from a more realistic representation. In this study, this process is the wave generation by wind. Figure 3-3 shows the feedback loop associated with this wave process. This momentum exchange is highly dependent on the provided wind field and the accurate parameterizations of the roughness length. Many different parameterizations exists for z_0 and a parameterization which accounts for all environmental conditions has still to be found. In this study, two roughness length parameterizations are included. The Charnock relation is used in many different atmospheric models, however it is only dependent on the friction velocity. Taylor and Yelland's relation is fully dependent on the sea state by its dependence on the significant wave height and wave length of the waves.

6-3-1   Parameterizations

The two parameterizations were characterized by Simulation 1C-B and 2C-B, to account for wind wake effects, caused by the wind turbines, and its subsequent impact on the sea state. As expected, the implementation of GRASP wind fields showed a substantial impact on the sea state behind the wind wake caused by the wind turbines (Figure 6-10).
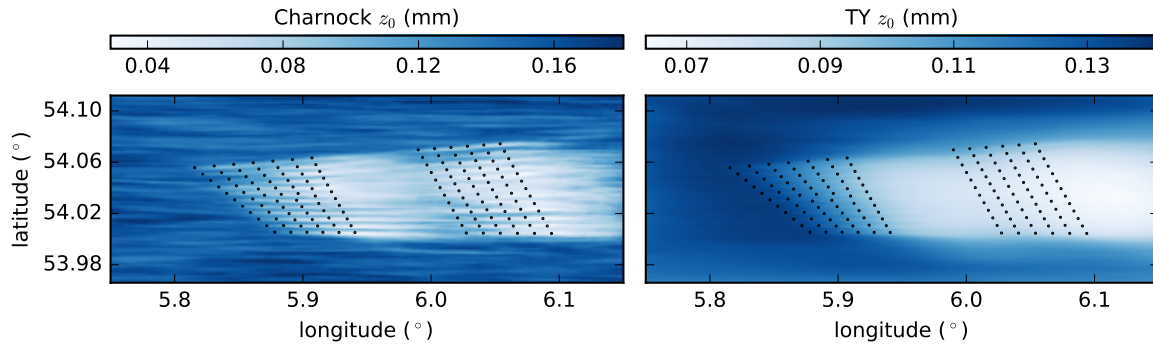
Figure 6-10: Contour plot of the difference in roughness lengths in the offshore wind farm area (Gemini). The contours are taken from the same moment in time; 2017, February 19, 10:30 UTC. The graph on the left is obtained from simulation 1C-B, the graph on the right is obtained from simulation 2C-B. The contour plot on the left hand side shows a roughness length which is fully dependent on the friction velocity (Charnock (1955); Charnock). On the right hand side, the contour plot is fully dependent on the sea state (Taylor and Yelland (2001); TY).

The amount of decrease in the z_0 field varies amongst the different two roughness length definitions. The Charnock (1955) relation shows a similar field compared to the wind speed, where the advection pattern and nudging zones can be clearly identified. By looking at the Taylor and Yelland (2001) contour plot, the impact of the wind wake is clearly identified. Moreover, the delayed decrease in roughness length is also clearly identified, because these effects only start to become significant at the fourth row of the streamwise turbines.

Figure 6-10 demonstrates the effect of a wind farm wake on the atmospheric roughness length. However, this contour plot is just a snapshot at a particular time. If the amount of evaluated timestamps were to be increased, a better picture should arise between the differences in roughness lengths of the two provided parameterizations. Therefore, for all pixels in the domain, at every time stamp of the simulation, the roughness length was constructed. This was done using the modelled friction velocities (u_*), peak phase speeds of waves (c_p), significant wave heights (H_s) and the wave lengths (L_{wave}), corresponding to the mean absolute wave period (T_{m-10}), at every grid point in the domain. Figure 6-11 shows the two roughness lengths which occur in the whole simulation, in time and space.

From Figure 6-11 on the following page, it can be identified that the Taylor and Yelland (2001) parameterization has a higher average roughness length, 3.7×10^{-4} m compared to 2.8×10^{-4} m for the parameterization of Charnock (1955). Moreover, the expression also provides values for z_0 lower than 10^{-7} in some exceptional cases. The peak roughness lengths of the simulations lie in the range between $10^{-4} < z_0 < 10^{-3}$, indicating a typical ocean sea surface (see Table 3-1).
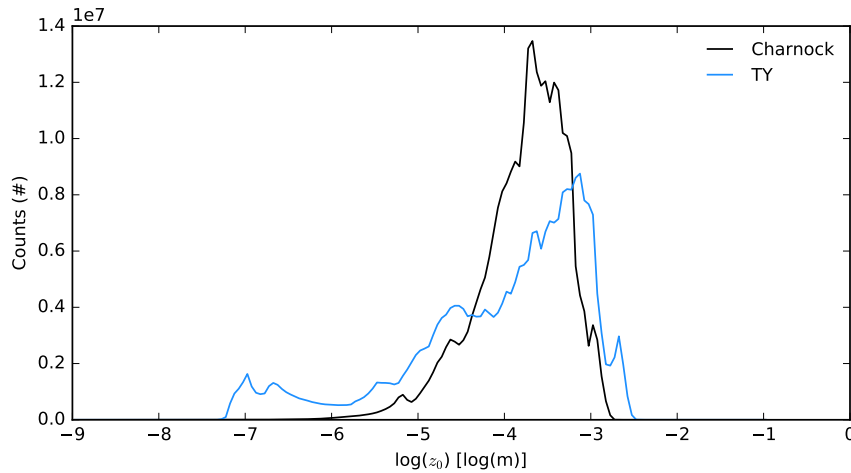
Figure 6-11: Distribution of the two roughness lengths, obtained form simulation 1C-B and 2C-B.

6-3-2   Characterization

To assess whether the distributions of the other simulations (1C-A, 1C-A, 2C-A, 2C-B) are different, all z_0 distributions of the simulations are constructed trough the Taylor and Yelland (2001) parameterization (TY). Figure 6-12 shows these different distributions.
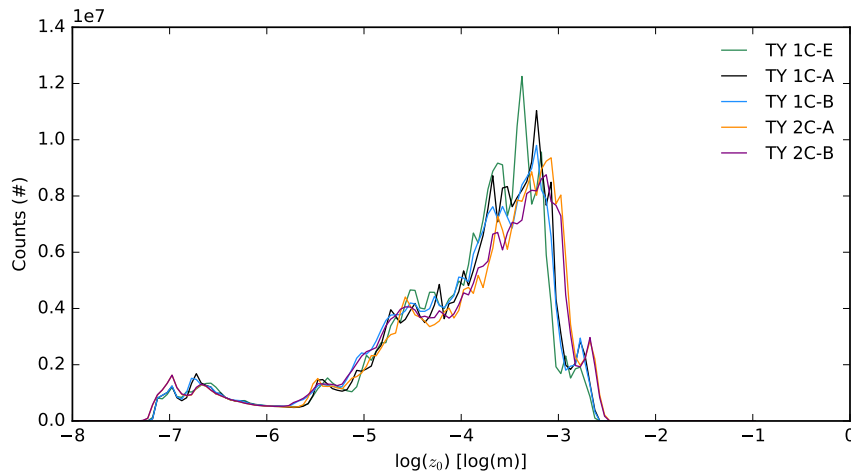
Figure 6-12: Distribution of Taylor and Yelland (2001) scaling for the different simulations.

The reason why this relation was chosen is twofold. First, the relation is fully sea state dependent, which therefore does not suffer from spurious correlation in u_*. Second, simulations 2C-A and 2C-B (the two-way coupled simulations) were coupled through the Taylor and Yelland (2001) parameterization and therefore the distributions were compared through the same scaling. As can be seen in Figure 6-12, the different distributions are matched quite evenly. One would expect slightly different z_0 distributions between the simulations with and without turbines. Providing an increase in counts for the smaller z_0 values for simulations

performed in a configuration with more heterogenic effects, e.g. offshore wind farms.
To identify the differences between the two parameterizations in relation to the friction veloc-
ity, and the possible identification of heterogenic effects on the z_0 field in the simulation with
turbines, four scatter plots were constructed. The direct impact of the friction velocity (u_*)
on the simulations, and the corresponding roughness lengths, are presented in Figure 6-13.
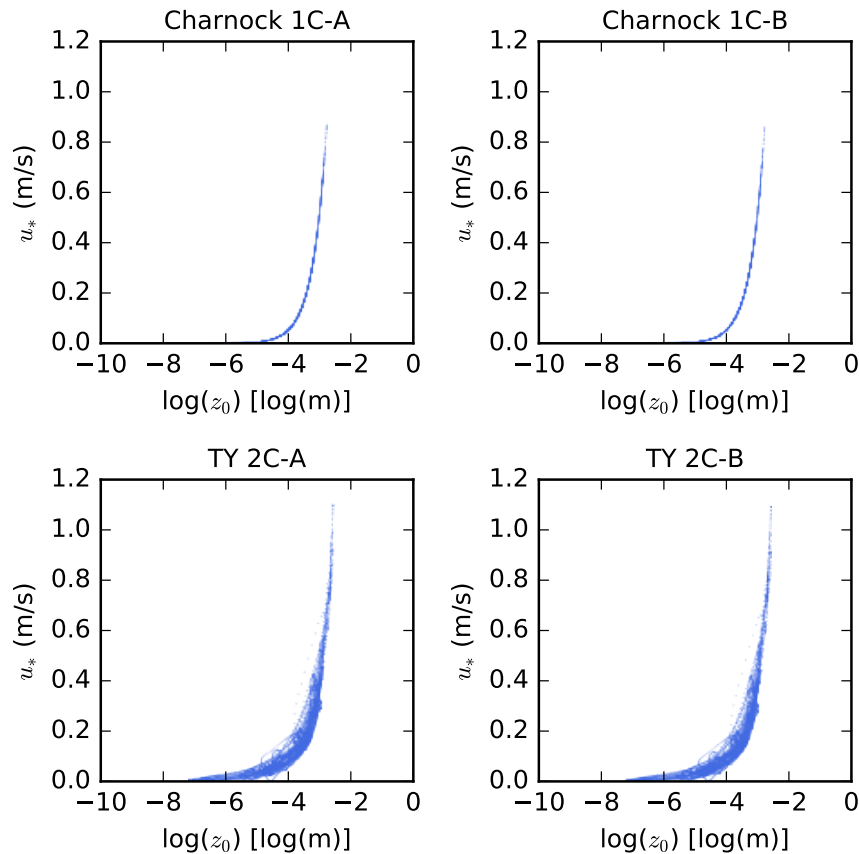
Figure 6-13: Scatter plots of the relation between z_0 and u_*. The values for z_0 and u_* are
spatially averaged over the entire domain for each time stamp. The scatter plots above contain
the roughness length for the one-way coupled simulations (1C-A and 1C-B), the scatter plots
below contain the roughness length for the two-way coupled simulations (2C-A and 2C-B).

As can be seen, the top two figures follow Charnock's relation (Equation 3-35). However, no
direct differences can be identified between simulation 1C-A and 1C-B regarding heterogenic
effects in moderate wind speeds. The figures below follow a more spread scatter because of
their dependency on multiple- or indirectly derived parameters. No direct differences were
identified here either, between simulation 2C-A and 2C-B, regarding heterogenic effects in
moderate wind speeds. Furthermore, the spatially- and time averaged roughness lengths for
the two-way coupled simulations are higher than the one-way coupled simulations (see Table
6-1). The next sections will elaborate further on the consequent drag coefficients and their
effect on the wind profiles.

6-3-3   Impact on atmosphere

To assess whether the two different parameterizations provide a different drag relation, and if this drag is influenced by a reduced z_0 field under the influence of heterogenic effects, the drag relations of the different simulations have been computed (Figure 6-14).
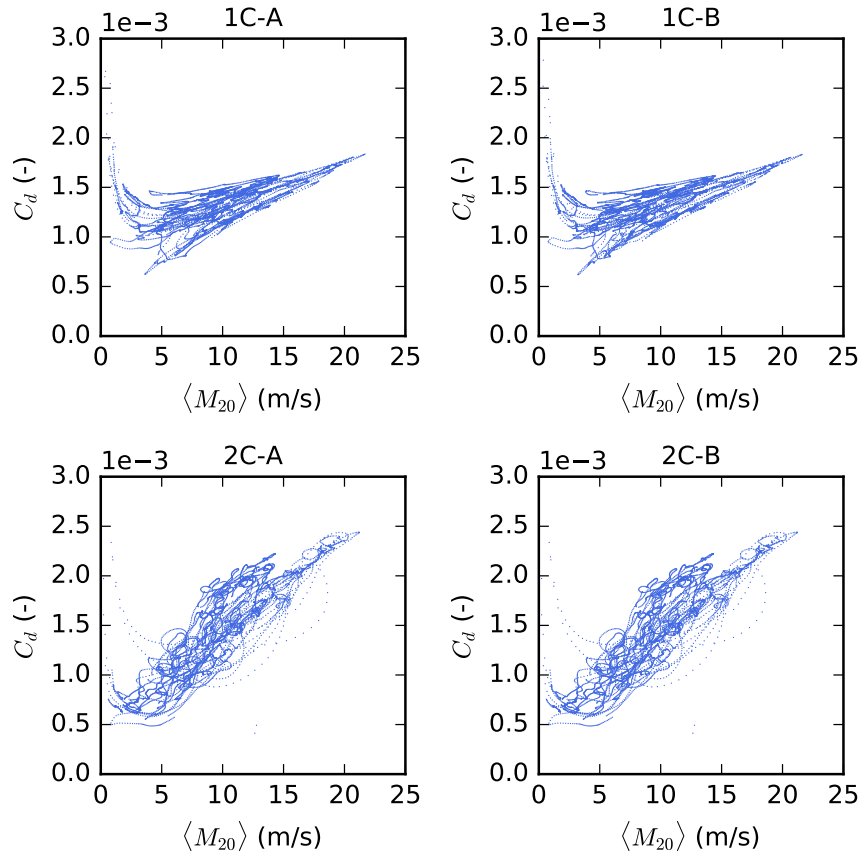
Figure 6-14: Drag relations for the different simulation cases. The drag coefficients are obtained by the slab averaged values for the friction velocities and the 20 meter wind speeds.

As expected, the drag coefficients increase for higher wind speeds in all simulations. The effect is stronger for the Taylor and Yelland (2001) formulation, used in simulation 2C-A and 2C-B, than the Charnock (1955) formulation, used in simulation 1C-A and 1C-B. This indicates that the two-way coupled simulation causes more momentum transfer to the atmosphere.

The four simulations have a high drag for very low wind speeds, and all having a minimal drag coefficient at a wind speed of around 5 m/s. The minimum is lower for the simulations performed with the parameterization of Taylor and Yelland (2001). But, the time- and spatially averaged drag coefficients of the two-way coupled simulations are higher than the one-way coupled simulations (see Table 6-1). This in line with the averaged roughness lengths of the different simulations, a higher roughness length provides a higher drag coefficient.

Table 6-1: Time- and slab averaged values for the roughness lengths and drag coefficients of the performed simulations.

	IC-A	IC-B	2C-A	2C-B
$\overline{z}_0$ (m)	$2.94 \cdot 10^{-4}$	$2.77 \cdot 10^{-4}$	$3.92 \cdot 10^{-4}$	$3.68 \cdot 10^{-4}$
$\overline{C}_d$ (-)	$1.33 \cdot 10^{-3}$	$1.32 \cdot 10^{-3}$	$1.44 \cdot 10^{-3}$	$1.43 \cdot 10^{-3}$

It can also be deduced from Table 6-1 that heterogenic effects have an impact on the time- and slab averaged values for the roughness length and drag coefficients. These two factors affect the time- and slab averaged wind profiles in the domain, which is presented in Figure 6-15.
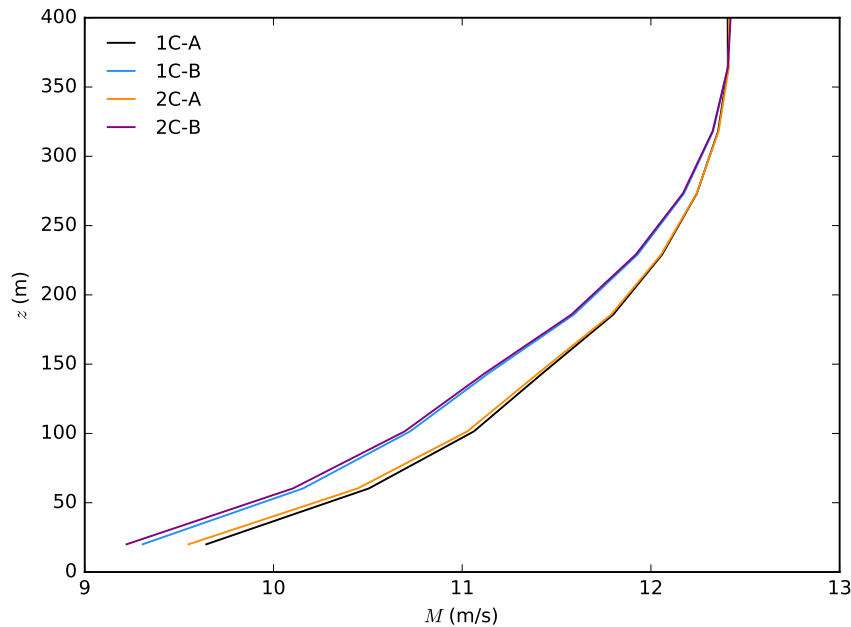
Figure 6-15: Time- and slab averaged wind magnitude profiles of the performed simulations.

As expected, the time- and slab averaged wind profiles for the simulations with turbines (1C-B and 2C-B) are reduced. Furthermore, the wind velocities for both two-way coupled simulations are further reduced at lower model levels, although small, in comparison with the one-way coupled simulations. This shows that the increased drag for the two-way coupled simulations, as presented in Figure 6-1, leads to increased roughness lengths. However, the friction velocities are increased for the two-way coupled simulation (Figure 6-8). This is explained by Section 3-4-2, where is stated that the friction velocity at the bottom boundary is determined by a different procedure. If the roughness length for momentum is increased in Equation 3-30 (assuming neutral stability conditions), and the other parameters do not change in comparison to the one-way coupled simulations, the friction velocity in Equation 3-32 is increased. This is also confirmed by Figure 6-13.

6-4   Assessment of hindcast performance

In the previous sections, the differences between the performed simulations were identified
and characterized. This section focuses on assessing the hindcast performance of the different
simulations.

6-4-1   Validation of significant wave height

In this section, the general performance concerning the prediction of the significant wave
height is assessed of ERA5 and simulation 1C-E up to and including 2C-B. This was done
by comparing H_s with observations from the offshore high voltage station present in the
wind farm. The GCM hindcast that was used in this study, ERA5, is also included in the
assessment to provide a benchmark for the simulations. The observations, with a time stamp
of 15 minutes, and the simulations, with a time stamp of 10 minutes, were all hourly averaged.
The data obtained from ERA5 was already provided in time stamps of one hour.
Although both SWAN and ERA5 outputs contain detailed information of the sea state over
the entire wind farm domain, the validation is restricted to one certain location, the location
of the offshore high voltage station BG were the observations are being performed. Also, only
the most relevant parameters (M, H_s) are being validated. Although the simulations were
only performed for the fist two months of 2017, a reasonable picture should be obtained of the
performance of each hindcast. On the next page, the associated scatter plots are presented
(Figure 6-16)
As can be seen, the scatter plots of ERA5 and the performed simulations do not provide a
visible distinction between the simulations. Therefore, a statistical analysis of ERA5 and the
simulations is done in order to provide a clearer picture of the associated skill performances.
In Table 6-2, this analysis is represented. Appendix B contains more information about the
statistical indicators used in this study.

Table 6-2: Statistical assessment of hindcasted significant wave height (H_s) at the BG OHVS
in Gemini, The Netherlands, of the first two months of 2017. All data was hourly averaged. N is
the total amount of data comparisons, σ is the standard deviation, MAE is mean absolute error,
MSE is the mean squared error, RMSE is the root mean squared error, r is the Pearson correlation
coefficient and R^2 is the coefficient of determination.

Model	N	Bias (m)	σ (m)	MAE (m)	MSE (m)	RMSE (m)	r (-)	R^2 (-)
ERA5	1405	0.0151	0.2639	0.1836	0.0699	0.2643	0.9795	0.9520
1C-E	1405	-0.0649	0.3027	0.2155	0.0958	0.3096	0.9775	0.9342
1C-A	1405	-0.0364	0.2907	0.2055	0.0858	0.2929	0.9780	0.9411
1C-B	1405	-0.0603	0.2871	0.2036	0.0861	0.2934	0.9786	0.9409
2C-A	1405	0.0060	0.2846	0.2056	0.0810	0.2846	0.9760	0.9444
2C-B	1405	-0.0197	0.2794	0.1994	0.0785	0.2801	0.9770	0.9461

The main results of Table 6-2 can be summarized as follows; the two-way coupled simulation
(2C-B) shows a reduced root mean square error (RMSE) when compared to the one-way
coupled simulation (1C-B). Indicating that the two-way coupled configuration could be an

improvement of performance skill in a high resolution configuration. Furthermore, the variance in the error of all simulations is the main contributor to the total error. There is no large systematic deviation (bias) in the simulations (Appendix B).

Nevertheless, both the one-way- and two-way coupled simulations are outperformed by ERA5 in terms of the statistical indicators presented in Table 5-2. However, ERA5 hindcasts combine observations into estimates using advanced data assimilation. Therefore, comparing the performed simulations with ERA5 is in essence the same as comparing simulation results with observational data. It can also be deduced from Table 6-2 that the simulations perform better each coupling configuration.
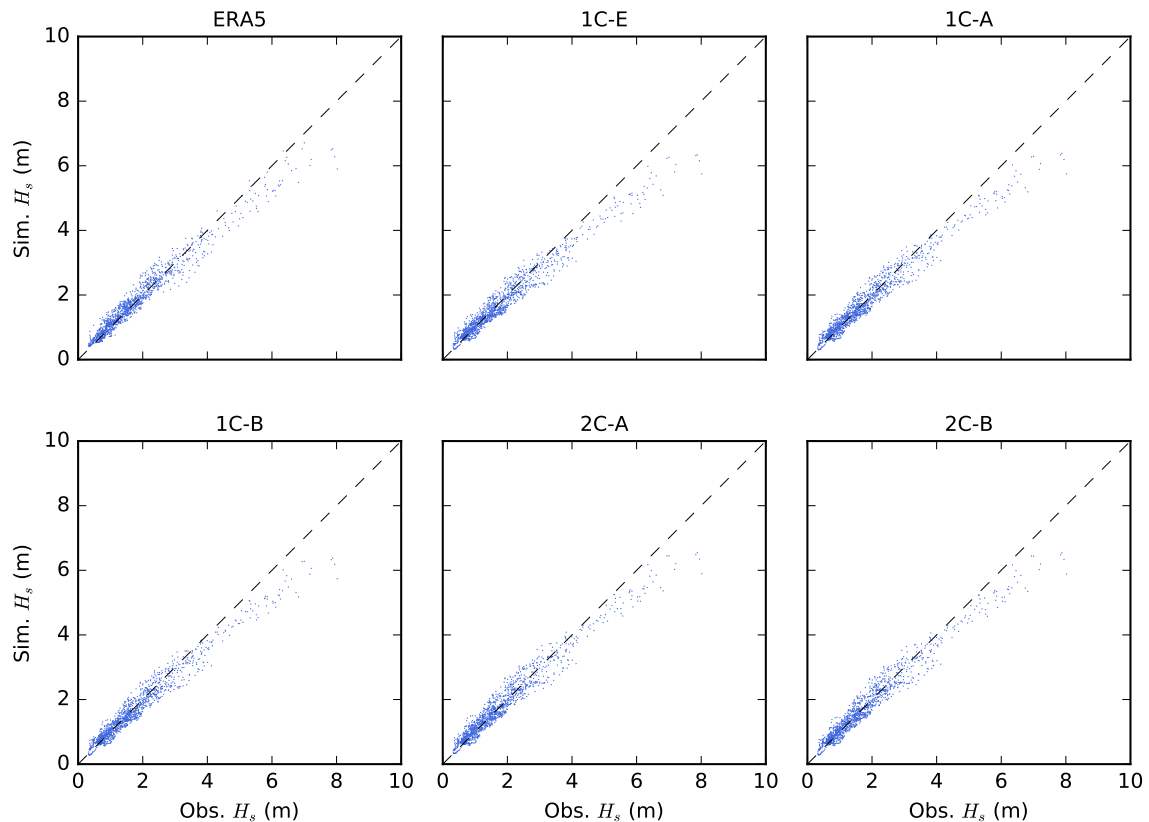
Figure 6-16: Scatter plots showing the simulated H_s in comparison with the observed H_s.

Moreover, Figure 6-17 shows the time series of the significant wave height for the observations, ERA5 and simulation 2C-B during the fist two months of 2017 at the BG offshore high voltage station. By reviewing these time series, a conformation can be given to the fact that the error does not appear to be clearly biased. However, both ERA5 and Simulation 2C-B underestimate high values by more than 1 meter for the significant wave height, as can be seen in Figure 6-17 and Figure 6-16. Furthermore, it can not be identified that the error in the significant wave height of Simulation 2C-B is reduced at the typical significant wave height regime where wave wakes could occur. However, as was identified in Figure 6-9, the magnitude of this possible wave deficit is also really small compared to the significant wave height.

As identified in Table 6-2, the performance of the coupled simulations is increased in comparison to simulation 1C-E. Besides the fact that the modelling performance is increased by the coupled configuration of an atmospheric large-eddy simulation and a spectral wave model, limiting factors are present. Section 6-5 elaborates further on these possible other factors which could be of influence.
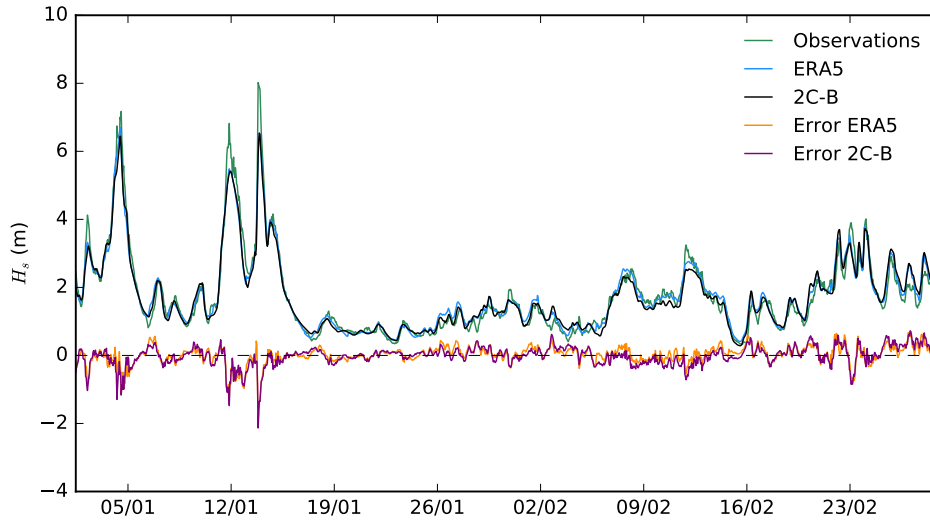
Figure 6-17: Time series of H_s at the location of the BG offshore high voltage station by ERA5, Simulation 2C-B and the observations.

6-4-2   Validation of wind velocity

The performance of the coupling configurations is further analyzed by validating the wind velocity magnitude of ERA5 and simulations 1C-B & 2C-B to the observations of the BG offshore high voltage station at an altitude of 46 meters above sea level. The observations, with a time stamp of 10 minutes, and the simulations, also with a time stamp of 10 minutes, were all hourly averaged. The data obtained from ERA5 was already provided in time stamps of one hour. Here, it should also be noted that only the first two months of 2017 were validated. Figure 6-18, on the next page, shows the associated scatter plots.

As can be seen, the scatter plot of the ERA5 wind field contains over prediction observed in the wind wake regime (6-12 m/s), caused by the thrust curve of the present wind turbines. This shows that the ERA5 wind fields do not take wake effects into account. Furthermore, such a bump is not identified in the one- and two-way coupled simulations.

To asses whether the wind field of the GRASP simulation is increased in performance by the momentum exchange with the spectral wave model (creating a sea state dependent roughness length), simulation 1C-B and 2C-B were also validated against the observations. The wind fields were obtained from certain model levels of both simulations. In this validation the wind fields at the first- and second full level of the simulations were used, 20 and 60 respectively, and logarithmically interpolated to a height of 46 meters. Table 6-3, on the next page, contains the statistical assessments.

Figure 6-18: Scatter plots of the wind velocity magnitude at an altitude of 46 meter.

Table 6-3: Statistical assessment of hindcasted wind velocity magnitude (M) at 46 meter height. At the BG OHVS in Gemini, The Netherlands, of the first two months of 2017. All data was hourly average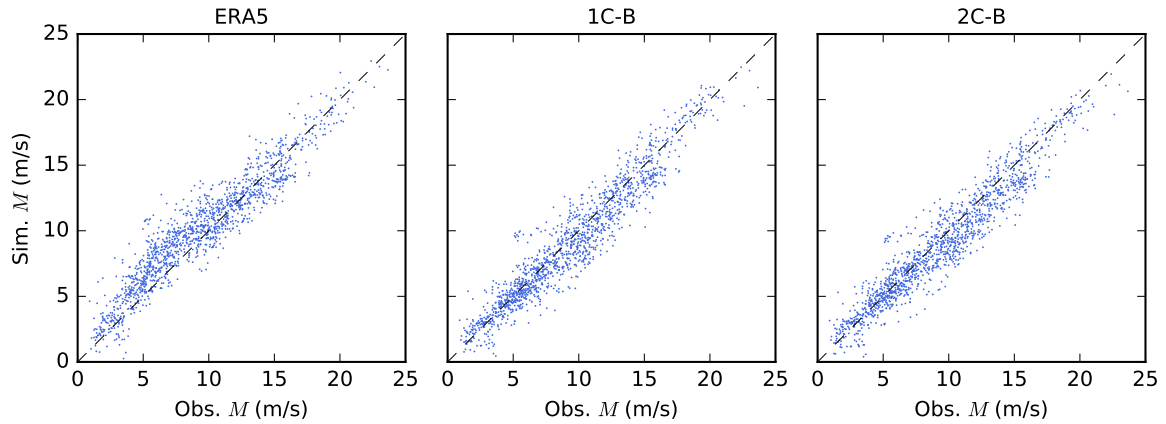d. N is the total amount of data comparisons, σ is the standard deviation, MAE is mean absolute error, MSE is the mean squared error, RMSE is the root mean squared error, r is the Pearson correlation coefficient and R^2 is the coefficient of determination.

Model	N	Bias (m/s)	σ (m/s)	MAE (m/s)	MSE (m/s)	RMSE (m/s)	r (-)	R^2 (-)
ERA5	1415	0.6736	1.4774	1.2836	2.6365	1.6237	0.9463	0.8714
1C-B	1415	-0.3025	1.3180	1.0411	1.8288	1.3523	0.9571	0.9108
2C-B	1415	-0.4131	1.3091	1.0582	1.8844	1.3727	0.9573	0.9081

The main results of Table 6-3 can be summarized as follows. Simulations 1C-B and 2C-B show an improvement on all statistical indicators when compared to ERA5. However, the two-way coupled simulation (2C-B) shows an increased bias and root mean square error (RMSE). The standard deviation (σ) is reduced, meaning that the variance is smaller around the average error. Therefore, the Pearson correlation coefficient (r) is increased. Furthermore, the increased bias and reduced variance show that the roughness length feedback to the atmospheric surface layer causes a more systematic under prediction (negative bias). This indicates that the roughness length parameterization of Taylor and Yelland (2001) causes an over prediction in momentum exchange.

6-5   Discussion

This study assesses the use of atmospheric large-eddy simulations, coupled to a spectral wave model, to enhance modelling of the roughness length and sea state. Furthermore, it investigates the impact on the performance of both the atmospheric- and spectral wave model. The results indicate substantial impact on these factors. However, before concluding the research regarding these factors, the limitations on this research need to be addressed.

It can be stated that one of the major effect of a more accurate and realistic representation of the atmospheric conditions, discussed in Section 6-4, resulted in an apparent performance

enhancement on the concerning oceanic conditions (the significant wave height) in comparison to simulation IC-E, which was clearly identified by Table 6-2. Therefore, the momentum exchange proved to be an apparent benefit for the oceanic side of the integrated numerical simulations. Although the turbulence-resolved wind field of simulation 1C-B and 2C-B outperformed the ERA5 wind field, ERA5 outperformed the other simulations concerning the estimate of the significant wave height. However, ERA5 combines observations into estimates using data assimilation. Therefore, comparing the performed simulations with ERA5 is in essence the same as comparing simulation results with observational data. It is more fair to compare the coupled simulations with simulation 1C-E.

Concerning the wind velocity, the hindcast performance is decreased from simulation 1C-B to simulation 2C-B. However, the standard deviation is reduced and the Pearson correlation coefficient is increased for simulation 2C-B. Because the bias is increased, a systematic under prediction could have arisen in simulation 2C-B which is caused by the chosen roughness length parameterization. This shows that the performance of the two-way coupled simulation is sensitive to the roughness length parameterization.

Nevertheless, it is still useful to address the observed drop in performance of simulation 1C-E (Table 6-2) in comparison to ERA5 concerning the significant wave height. Therefore, possible limitations are identified. First, the boundary conditions of the nested area (small domain) should be in perfect order to obtain the most realistic wave energy spectrum. These boundary conditions could be influenced by many factors, where the most important are, (1) the input parameters (H_s, T_p, θ_{mean}, m) provides to the SWAN simulation of the large domain and (2) the lasting influence of ERA5 wind fields on the wave spectrum on the large simulation domain.

Considering the input parameters, as was discussed in Section 5-4-2, these were obtained from ERA5. The significant wave height, peak period and mean wave direction were directly forced to the spectral wave model. However, the necessary power of the directional spreading had to be translated from ERA5's spectral directional width according to Equation 2-10. However, this relation is incorrect, where the alternative is to provide the spectral directional width (σ_θ) directly to spectral wave model. However, the impact of such an incorrect boundary condition should be considerably small if the nested simulation is sufficient far off the boundaries of the large domain, as was the case in this research.

Secondly, besides the boundary- and initial conditions, also the nature of ERA5's model could be of influence. The integrated oceanic spectral wave model in ERA5 could perform better on the large domain in this study. Also, the model of ERA5 contains advanced statistical post-processing which cannot be matched by the presented physical simulations.

Other limitations concern the two-way coupled simulations. First, the concurrent cursor-precursor method used in the atmospheric large-eddy simulation GRASP is very useful for atmospheric applications. However, the nudging zones in the cursor simulation actually influence the spectral wave simulation if the domain is equal to LES domain. Therefore, the nudging zones of the LES could force higher waves in the nested domain. Furthermore, in a two-way coupled configuration, the nudging zones interfere with the present momentum exchange. If also a two-way coupled precursor simulations was setup, this interference could be solved. Secondly, because in this research the spectral wave model could not provide all parameters, some needed to be derived. The coupling parameterization used in this study (Taylor and Yelland, 2001) uses the wave steepness, therefore the peak wave length needed to be obtained. However, this parameter is derived using the dispersion relation, by obtaining the mean absolute wave period (T_{m-010}).

Furthermore, a main limitation of this research concerns the simulation period. Because of computational costs, only a simulation period of two months was performed. A longer period of validation incorporates many different atmospheric- and oceanic conditions, which results in a more thorough statistical assessment.

Moreover, the LES contains several sources of uncertainty, such as the subgrid model and the initial conditions. Also, the spin-up of the GRASP simulations require initialization with random perturbations to drive the atmospheric turbulence. These random perturbations possibly could affect the obtained results. In meteorology, these uncertainties are addressed by performing multiple simulations of the setup with slightly changed initial values, creating ensembles. These ensembles are however not taken into account in this study.

Chapter 7

Conclusions and Recommendations

7-1 Introduction

In this chapter a recapitulation is presented of the main results of this research project. Moreover, as this study leaves behind interesting research opportunities for future work, some directions are listed for further research in line with metocean- forecasting and hindcasting. In Section 7-2, the main conclusions are stated and in Section 7-3 the recommendations for future research are presented.

7-2 Conclusions

The objective of this master thesis is to *assess and advance atmospheric large-eddy simulations coupled to a spectral wave model for enhanced operational metocean forecasting in offshore wind farms*. To meet this objective, the scope of the work is divided into four parts: (1) to assess the large-scale-, LES- and spectral wave model on its performance and to provide a benchmark for the two-way coupled simulations, (2) to establish a method for coupling an atmospheric LES to a spectral wave model, (3) to identify heterogenic effects on the sea state and atmospheric roughness length by performing coupled simulations and (4) to investigate one-way- and two-way coupling of an atmospheric LES to the spectral wave model in a quantitative manner. First, a more in-depth conclusion is presented of each part of the work. Second, the main conclusion of the research objective is provided.

Section 6-4 provides the performance assessment of ERA5, the atmospheric LES and the spectral wave model. It was found that the ERA5 wave field outperformed SWAN when forced by an ERA5 wind field. This drop in performance is explained by the different physical nature of the ERA5 model and SWAN model. Because ERA5 is based on observations and data assimilation, it is more appropriate to compare the coupled simulations to the SWAN simulation for by ERA5 wind fields (simulation IC-E). Moreover, an over estimation of ERA5 wind fields was identified at moderate wind velocities. Indicating that wake effects are not

taken into account. The atmospheric LES did not include these over estimations, proving it resolves the wind farm wake effects. Furthermore, limitations regarding the input boundary conditions for the spectral wave model were identified.

Section 5-5 elaborates on the one- and two-way coupling of the atmospheric large-eddy simulation GRASP and the spectral wave model SWAN. Both coupling configurations were established in this study. The one-way coupling is established by providing LES pseudo wind fields to SWAN. Here, the pseudo wind fields are derived from the friction velocities of the LES model, using the inverse of the Wu (1982) relation. The two-way coupling is established by providing SWAN to ASPIRE, where the momentum parameters u_* and z_0 are exchanged each coupling time step, using the parameterization of Taylor and Yelland (2001).

Section 6-3 focuses on the characterization of the roughness lengths presented in this study. It was found that the wind- and wave wake effects reduce the value of the roughness length for the two parameterizations. The relation of Charnock (1955) closely follows the wind field, the Taylor and Yelland (2001) relation follows the more realistic profile of the sea state. A clear difference in z_0 distributions for the different simulations cases was however not found. Therefore, Section 6-2 further identified the conditions for the observed heterogenic effects. It is concluded that the spatially averaged wave deficit follows the same pattern as the magnitude of the thrust curve of the wind turbines in neutral atmospheric stability conditions. Moreover, if the wind- and wave directions are aligned, favourable conditions arise for wave reduction. In addition, the spatially averaged wave deficits increased in magnitude by running in the two-way coupled configuration. This originates from the fact that, on average, the friction velocities are higher in the two-way coupled configuration due to a higher average value for the roughness length. This leads to a higher drag coefficient and subsequent wave growth and wave reduction. However, the observed peak wave wakes were in the order of 4.5 centimeters, which is small compared to a significant wave height of several meters.
Furthermore, the higher drag coefficients for the two-way coupled simulations resulted in a reduced time- and slab averaged wind profile.

Following the validation of the large-scale-, LES- and spectral wave model, the performance of the one- and two-way coupled simulations is also presented in Section 6-4. By comparing the significant wave height of the coupled simulations, running in hindcast mode, with the observations from the offshore high voltage station, the performance of the relevant modelled atmospheric- and wave conditions (M, H_s) were quantitatively evaluated. Generally, it was found that minor modelling errors are being made for the significant wave height. And the errors were reduced by the one-way coupled simulation and even more by the two-way coupled simulation, in comparison to simulation 1C-E. It is concluded that the one- and two-way coupled simulations were an advancement in modelling performance when compared to the SWAN simulation forced by ERA5 wind fields (simulation 1C-E). Therefore, it can be confirmed that there is added value for high-resolution metocean modelling. Although the modelling performance is improved, the benchmark hindcast (ERA5) provided the best performance. Besides the evaluated performance of the significant wave height, it is concluded that the two-way coupled simulations could be enhancement for the atmospheric model GRASP, but this is highly dependent on the implemented roughness length parameterization.

To conclude, the one- and two-way coupled simulations proved to be enhancement of a SWAN simulation forced by ERA5 wind fields in offshore wind farms. Furthermore, the two-way coupled simulation could be an improvement for an atmospheric large-eddy simulation.

7-3   Recommendations

Based on the performed research in this study, directions for further research are identified. These recommendations may be divided in two parts: (1) proposals regarding the further development of high-resolution metocean modelling and (2) suggestions for research in other area's where more advanced and consistent metocean forecasting and hindcasting could play a significant role.

- First of all, this study only performed simulations of the first two months of 2017. To provide really accurate and reliable conclusions on the statistical analysis, at least simulations of an entire year should be performed. Because part of this research was to advance the method of the one- an two-way coupled simulations, no long runs were undertaken. For future research, it is advised to perform such a full year analysis.

- Part of the reason to perform a full year analysis is to account for many different environmental conditions, because in this study only neutral stability conditions were observed. Furthermore, it can be deduced which simulation provides the most accurate representation in particular conditions. Therefore it is advised to study different atmospheric- and oceanic conditions and their impact on the coupled simulations.

- The SWAN wave model is famously known for its accurate performance in coastal waters (shallow waters). In this research, the spectral wave simulations were performed on a large area, covering a large part of the Dutch continental shelf, and a small area were the specific wind farm is located. The depth of the small area was already relatively deep (~ 30 meters). A specific limit to the performance of SWAN in deeper waters is not provided, however it is preferred to simulate in more coastal zones. Therefore it is advised to perform the presented simulations in a wind farm zone located close to shore and to identify the possible improvement in performance compared to ERA5. Another recommendation would be to nest the (coupled) SWAN simulation into spectral wave models more suited to oceanic waters (WAM or WAVEWATCH III), in order to identify if the boundary conditions benefit from this nesting.

- It would be enhancement if the spectral wave model were to be provided with time dependent currents and water levels. The first in order to provide the possibility to solve the action balance equation instead of the energy balance equation by the spectral wave model. The latter because it could have an impact on the simulated wave heights. Besides, data from an oceanic model could be used to improve the representations of the lower boundary conditions of the atmospheric model. In other words, to enhance the representations of the heat- and moisture flux into the atmosphere.

- Evaluation of the numerous parameterizations of the roughness lengths is necessary to assess the best representation of the momentum exchange to the atmospheric surface layer. As observed in this study, the sea state dependent roughness length appeared to perform better than the traditional Charnock relation in terms of its variance. Comparing different sea state dependent roughness lengths in the same configuration of a two-way coupled simulation, should provide interesting results.

- As identified in this study, the nudging zones of the atmospheric LES affect the representation of the actual wind field forced to SWAN. In this study, the precursor was

still simulated in an uncoupled configuration. It is therefore proposed to also setup a two-way coupled precursor simulation.

- In this research, ERA5 wind- and wave parameters were used to provide the initial- and boundary conditions to GRASP and SWAN. If these initial- and boundary conditions were replaced by ECMWF's IFS day-ahead forecast, also research can be conducted on the possible enhancement of predicting weather windows.

The recommendations for further research on the use of the two-way coupled simulations for other applications are twofold:

- First of all, the two-way coupled simulations can provide consistent high-resolution atmospheric- and oceanic data on the environmental conditions and subsequent loads on offshore wind turbines. It would be interesting to investigate the added value of these more consistent and higher resolution environmental data, in comparison to the traditionally used environmental data.

- Besides the recommendations to advance metocean modelling for enhanced offshore wind turbine engineering, installation and maintenance, modelling the interaction between the atmospheric surface layer and the ocean opens new doors for assessing the impact of the environmental conditions on the power production of offshore wind turbines. Considering a coupled configuration of an atmospheric large-eddy simulation, a spectral wave model and an oceanic model, the impact of momentum-, heat- and moisture exchange on the power production of offshore wind turbines can be investigated.

Appendix A

Results of two-way coupling

Within this Appendix, some additional results of the two-way coupled simulations regarding the conditioning of wave deficit are included. These results show similar behaviour as the results of the one-way coupled simulations presented in Chapter 6.
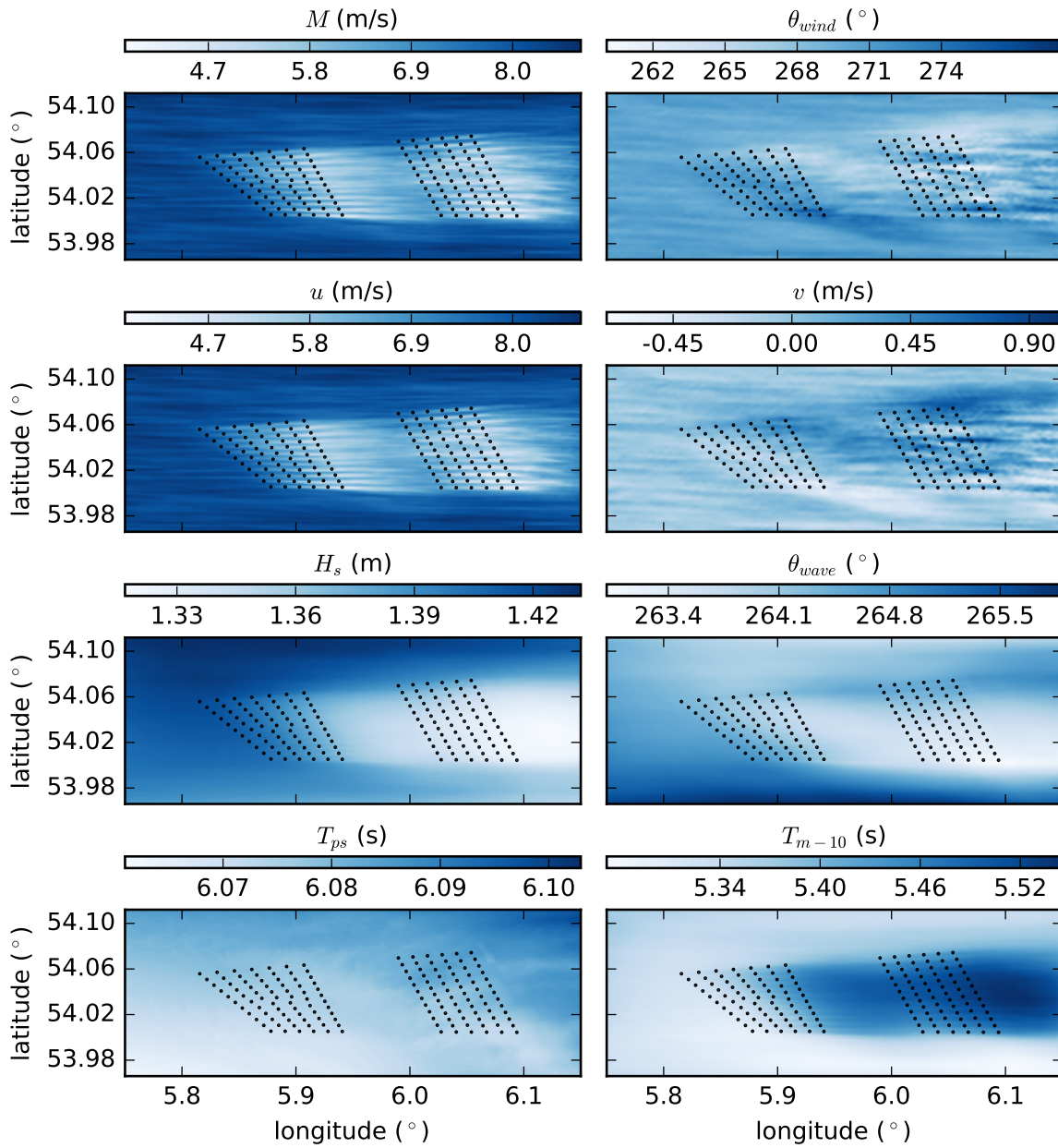
Figure A-1: Contour plots of the effects of wind turbines on a number of atmospheric- and ocean conditions. All contours are from the same moment in time: 2017, February 19, 10:30 UTC. The contour plots were obtained from simulation 2C-B, the two-way coupled GRASP/SWAN configuration.
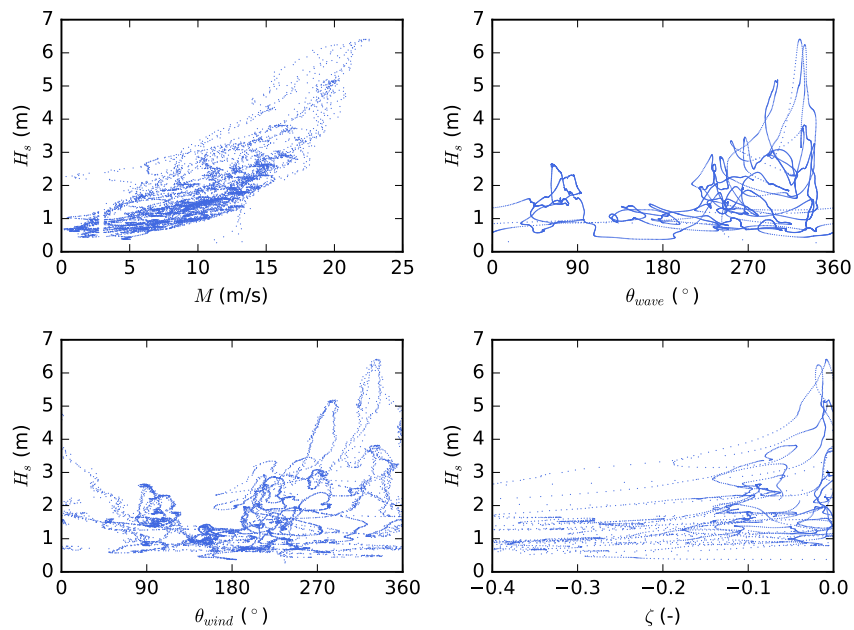
Figure A-2: Conditioning of the significant wave height (H_s) with the chosen parameters for the two-way coupled simulations.
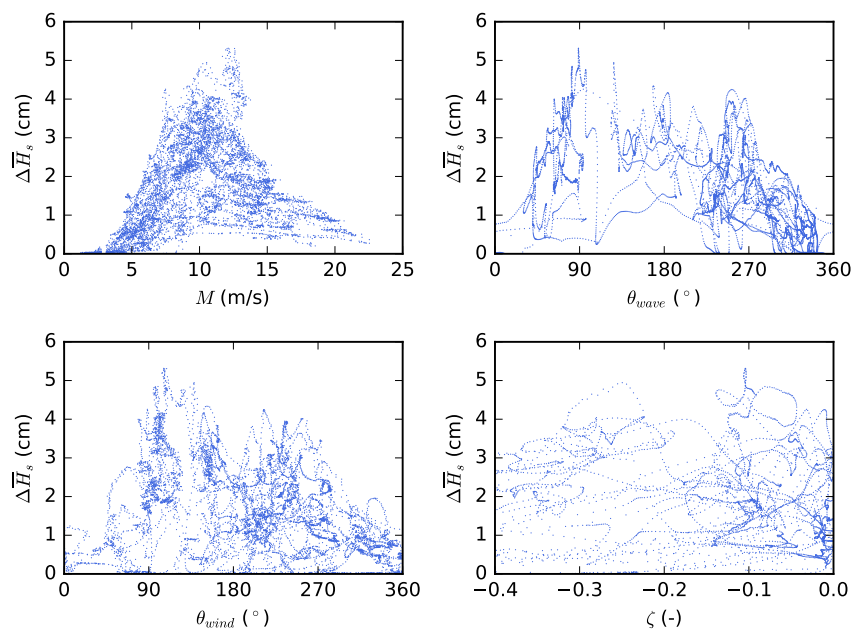

Figure A-3: Conditioning of the significant wave height deficit $(\Delta \overline{H}_s)$ with the chosen parameters for the two-way coupled simulations.
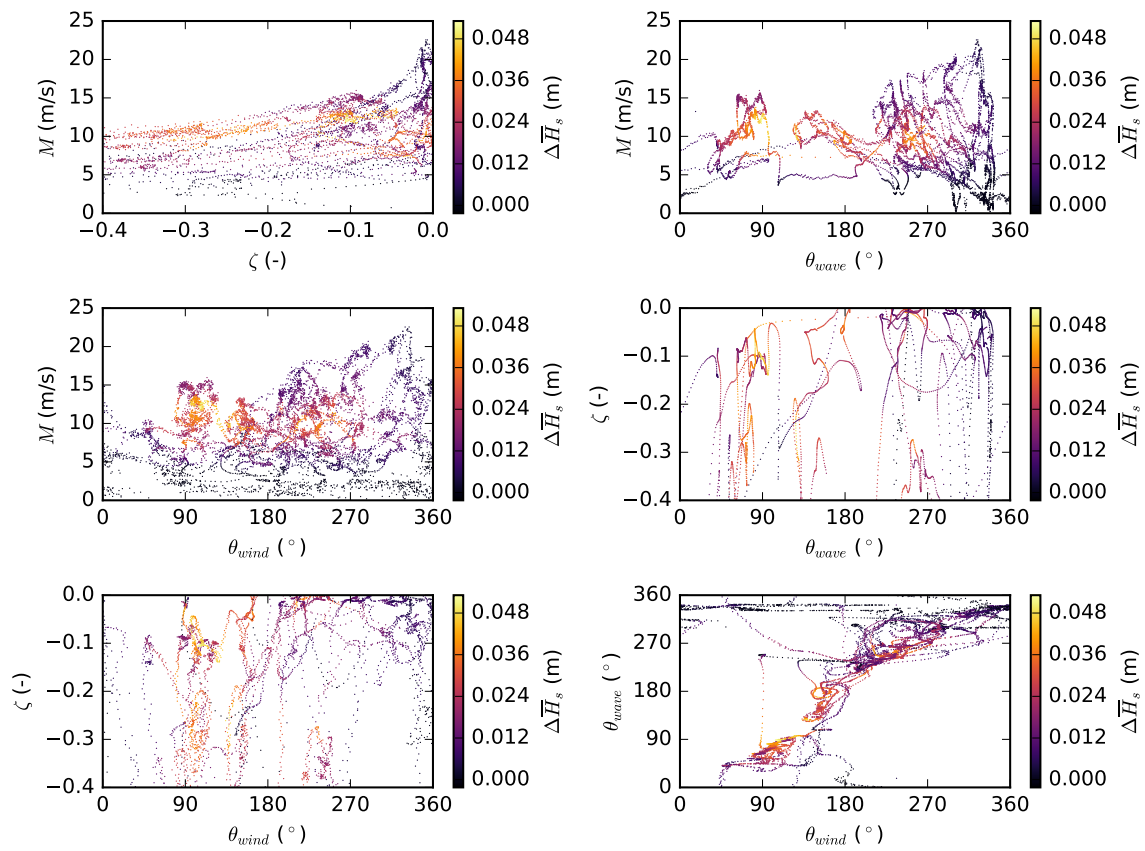
Figure A-4: Conditions for the occurrence of a decrease in average significant wave height by heterogeneous effects for the two-way coupled simulations.

Figure A-5: Average significant wave height deficit for each wind direction interval, for the two-way coupled simulations.

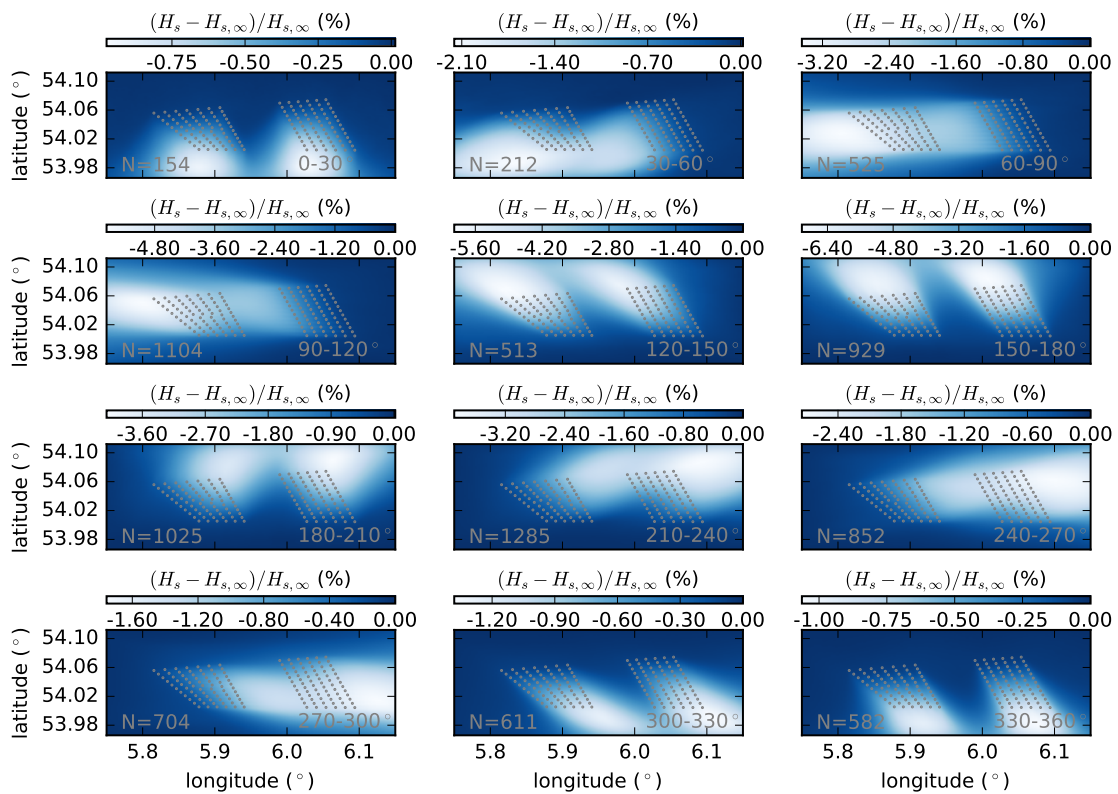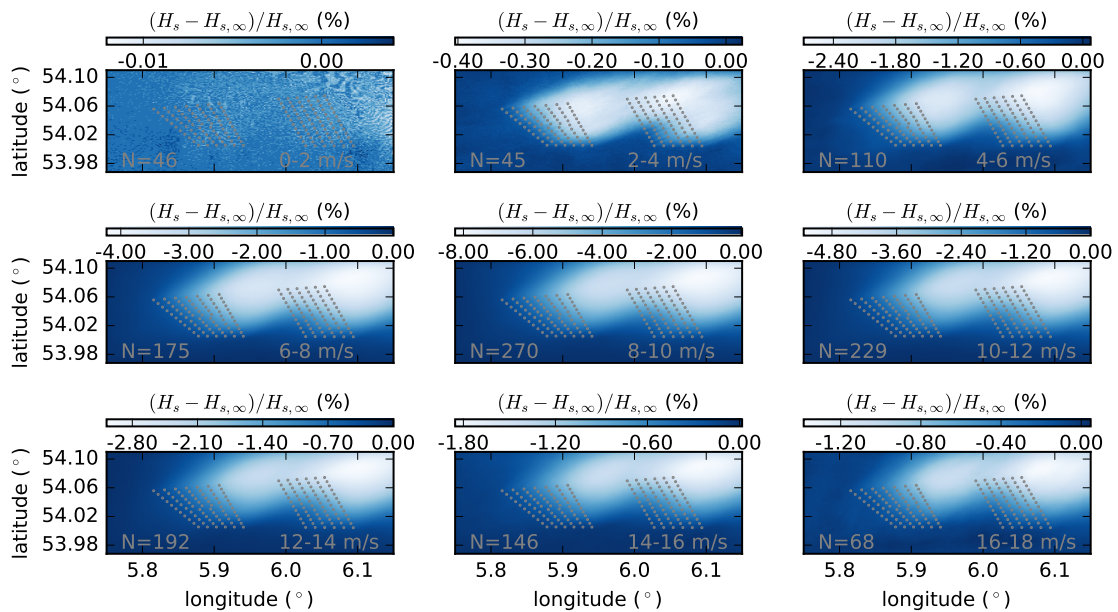**Figure A-6:** Average significant wave height deficit for each wind speed interval, considering wind from the southwest direction (210-240°), for the two-way coupled simulations.

Appendix B

Statistics

To assess the performance of atmospheric- and oceanic parameters with obtained observations, statistical indicators are used. They are used to analyse the quality of the performed simulations.

As stated by van Laarhoven (2019), the values of the simulated parameters are represented by $y = (y_1, y_2, y_3, ..., y_i)$ and the values of the observed parameters are represented by $x = (x_1, x_2, x_3, ..., y_i)$. The mean of these observed or simulated values is given by:

$$\overline{x} = \frac{1}{n} \sum_{i=1}^{n} x_i, \qquad \overline{y} = \frac{1}{n} \sum_{i=1}^{n} y_i \tag{B-1}$$

The error of the simulated variable, is given by the the difference in the simulated- and observed value ($e_i = y_i - x_i$). Where the bias is the mean of all these errors combined:

$$
\begin{aligned}
\text{Bias}(y, x) &= \frac{1}{n} \sum_{i=1}^{n} (y_i - x_i) \\
&= \frac{1}{n} \sum_{i=1}^{n} y_i - \frac{1}{n} \sum_{n=1}^{n} x_i \\
&= \overline{y} - \overline{x}
\end{aligned}
\tag{B-2}
$$

Because positive and negative errors cancel each other out, it is advised to use other statistical indicators for assessing a certain simulation. The mean absolute error (MAE) computes the magnitude of each error, therefore positive- and negative values cannot cancel each other out. It is defined by:

$$\text{MAE}(y, x) = \frac{1}{n} \sum_{i=1}^{n} |y_i - x_i| \tag{B-3}$$

Also, the mean squared error is similar to the MAE. However, it is squared before averaging:

$$\text{MSE}(y, x) = \frac{1}{n} \sum_{i=1}^{n} (y_i - x_i)^2 \tag{B-4}$$

The root mean squared error (RMSE) is the square rooted of the MSE:

$$\text{RMSE}(y, x) = \sqrt{\frac{1}{n} \sum_{i=1}^{n} (y_i - x_i)^2} \tag{B-5}$$

Furthermore, if the squared bias is subtracted from the squared RMSE, the variance is obtained (σ^2), where σ is the standard deviation:

$$\sigma = \sqrt{\frac{1}{n} \sum_{i=1}^{n} ((e_i - \bar{e})^2)} \tag{B-6}$$

This can be translated in the following, the RMSE consist of a systematic error (bias) and a random error (variance).

Also, the Pearson correlation coefficient (r) is a measure of the linear correlation between the two variables x_i and y_i (Taylor, 1997):

$$r(y, x) = \frac{\sum_{i}^{n} (x_i - \bar{x})(y_i - \bar{y})}{\sqrt{\sum_{i}^{n} (x_i - \bar{x})^2} \sqrt{\sum_{i}^{n} (y_i - \bar{y})^2}} \tag{B-7}$$

Lastly, the coefficient of determination (R^2) is a measure of how close the simulated variables are to the fitted regression line (Dodge, 2008):

$$R^2(y, x) = 1 - \frac{\sum_{i}^{n} (x_i - y_i)^2}{\sum_{i}^{n} (x_i - \bar{x})^2} \tag{B-8}$$

Bibliography

D. Allaerts and J. Meyers. Gravity Waves and Wind-Farm Efficiency in Neutral and Stable Conditions. *Boundary-Layer Meteorology*, 166(2):269–299, 2017.

T. Bon. Analysis of wind farm global blockage with large-eddy simulations. Master's thesis, Delft University of Technology, 2019.

N. Booij, R. C. Ris, and L. H. Holthuijsen. A third-generation wave model for coastal regions 1. Model description and validation. *Journal of Geophysical Research: Oceans*, 104(C4): 7649–7666, 1999.

L. Cavaleri and P. M. Rizzoli. Wind wave prediction in shallow water: theory and applications. *Journal of Geophysical Research*, 1981.

H. Charnock. Wind stress on a water surface. *Quarterly Journal of the Royal Meteorological Society*, 1955.

H. Charnock. A note on empirical wind wave formulae. *Quarterly Journal of the Royal Meteorological Society*, 1958.

R. H. Clarke. Observational studies in the atmospheric boundary layer. *Quarterly Journal of the Royal Meteorological Society*, 1970.

S. R. de Roode. Atmospheric physics. Syllabus, 2019.

J. W. Deardorff. A numerical study of three-dimensional turbulent channel flow at large reynolds numbers. *Journal of Fluid Mechanics*, 41(2):453–480, 1970.

Y. Dodge. *The Concise Encyclopedia of Statistics.* Springer, 2008.

W. M. Drennan, P. K. Taylor, and M. J. Yelland. Parameterizing the Sea Surface Roughness. *Journal of Physical Oceanography*, 35(5):835–848, 2005.

ECMWF. Era5 data documentation, 2019. URL https://confluence.ecmwf.int/display/CKB/ERA5+data+documentation.

EMODnet. Bathymetry: Understanding the topography of the european seas, 2019. URL https://www.emodnet-bathymetry.eu/.

EZK. Energieagenda, 2016. URL https://www.rijksoverheid.nl/onderwerpen/klimaatverandering/documenten/rapporten/2016/12/07/ea.

EZK. Klimaatakkoord, 2019. URL https://www.rijksoverheid.nl/onderwerpen/klimaatverandering/documenten/rapporten/2019/06/28/klimaatakkoord.

J. R. Garratt. Review of Drag Coefficients over Oceans and Continents. *Monthly Weather Review*, 1977.

J. R. Garratt. *The Atmospheric Boundary Layer*. Cambridge University Press, 1992.

G. L. Geernaert, K. B. Katsaros, and K. Richter. Variation of the drag coefficient and its dependence on sea state. *Journal of Geophysical Research*, 1986.

Gemini. The gemini offshore wind park, 2019. URL https://www.geminiwindpark.nl/.

K. Hasselmann, T. P. Barnett, E. Bouws, H. Carlson, D. E. Cartwright, K. Eake, J. A. Euring, A. Gicnapp, D. E. Hasselmann, P. Kruseman, A. Meerburg, P. Mullen, D. J. Olbers, K. Richren, W. Sell, and H. Walden. Measurements of wind-wave growth and swell decay during the joint North Sea wave project (JONSWAP). *Deutschen Hydrographischen Zeitschrift*, 1973.

T. Heus, C. C. Van Heerwaarden, H. J. Jonker, A. Pier Siebesma, S. Axelsen, K. Van Den Dries, O. Geoffroy, A. F. Moene, D. Pino, S. R. De Roode, and J. V. G. De Arellano. Formulation of the Dutch Atmospheric Large-Eddy Simulation (DALES) and overview of its applications. *Geoscientific Model Development*, 3(2):415–444, 2010.

M. Hintz. *Theoretical Analysis and Large-Eddy Simulations of the Propagation of Land-Surface Heterogeneity in the Atmosphere*. PhD thesis, Universtität zu Köln, 2016.

U. Högström. Non-dimensional wind and temperature profiles in the atmospheric surface layer: A re-evaluation. *Boundary-Layer Meteorology*, 42:55–78, 1988.

L. H. Holthuijsen. *Waves in oceanic and coastal waters*. Cambridge University Press, 2007.

M. C. Holtslag. *Far offshore wind conditions in scope of wind energy*. PhD thesis, Delft University of Technology, 2016.

P. A. E. M. Janssen, J. Bidlot, B. Hansen, L. Isaksen, and P. Viterbo. Impact and feedback of ocean waves on the atmosphere. *Atmosphere Ocean Interactions*, 1(August):155–197, 2002.

J. M. J. Journée and W. W. Massie. *Offshore Hydromechanics*. Delft University of Technology, 2001.

S. A. Kitaigorodskii and Y. Volkov. On the roughness parameter of the sea surface and the calculation of momentum flux in near-water layer of the atmosphere. *Izv. Atmos. Oceanic Phys.*, 1965.

B. Liu, H. Liu, L. Xie, C. Guan, and D. Zhao. A Coupled atmosphere-wave-ocean modeling system: simulation of the intensity of an idealized tropical cyclone. *Monthly Weather Review*, 139(1):132–152, 2011.

J. Meyers and C. Meneveau. Large Eddy Simulations of Large Wind-Turbine Arrays in the Atmospheric Boundary Layer. *48th AIAA Aerospace Sciences Meeting Including the New Horizons Forum and Aerospace Exposition*, pages 1–10, 2010.

J. W. Miles. On the generation of surface waves by shear flows. *Journal of Fluid Mechanics*, 1957.

C. Moeng and P. Sullivan. *Large-Eddy Simulation.* Encyclopedia of Atmospheric Sciences, 2002.

A. S. Monin and A. M. Obukhov. Basic laws of turbulent mixing in the atmosphere near the ground. *Tr. Akad. Nauk SSSR Geofiz. Inst*, 24(151):163–187, 1954.

W. Munters, C. Meneveau, and J. Meyers. Turbulent Inflow Precursor Method with Time-Varying Direction for Large-Eddy Simulations and Applications to Wind Farms. *Boundary-Layer Meteorology*, 159(2):305–328, 2016.

A. M. Obukhov. Turbulence in an atmosphere with a non-uniform temperature. *Boundary-Layer Meteorology*, 1971.

O. M. Phillips. On the generation of waves by turbulent wind. *Journal of Fluid Mechanics*, 1957.

W. J. Pierson, G. Neumann, and R. W. James. Observing and Forecasting Ocean Waves by Means of Wave Spectra and Statistics. *Hydrographic Office Publication*, 1955.

L. F. Richardson. *Weather prediction by numerical process.* Cambridge University Press, 1922.

C. Röckmann, S. Lagerveld, and J. Stavenuiter. *Operation and Maintenance Costs of Offshore Wind Farms and Potential Multi-use Platforms in the Dutch North Sea.* Springer, 2017.

J. Schalkwijk. *Toward turbulence-resolving weather and climate simulation.* PhD thesis, Delft University of Technology, 2015.

J. Schalkwijk, E. J. Griffith, F. H. Post, and H. J. J. Jonker. High-Performance Simulations of Turbulent Clouds on a Desktop PC: Exploiting the GPU. *Bulletin of the American Meteorological Society*, 93(3):307–314, 2012.

J. Schalkwijk, H. J. J. Jonker, A. P. Siebesma, and F. C. Bosveld. A Year-Long Large-Eddy Simulation of the Weather over Cabauw: An Overview. *Monthly Weather Review*, 143(3): 828–844, 2014.

J. Smagorinsky. General circulation experiments with the primitive equations. *Monthly Weather Review*, 91(3):99–164, 1963.

S. D. Smith and E. G. Banke. Variation of the sea surface drag coefficient with wind speed. *Quarterly Journal of the Royal Meteorological Society*, 1975.

R. L. Snyder, F. W. Dobson, J. A. Elliott, and R. B. Long. Array measurements of atmospheric pressure fluctuations above surface gravity waves. *Journal of Fluid Mechanics*, 1981.

R. J. Stevens, J. Graham, and C. Meneveau. A concurrent precursor inflow method for Large Eddy Simulations and applications to finite length wind farms. *Renewable Energy*, 68: 46–50, 2014.

R. B. Stull. *An Introduction to Boundary Layer Meteorology*. Kluwer Academic Publishers, 1988.

SWAN. Swan user manual cycle iii version 41.31, 2019. URL http://swanmodel.sourceforge.net/.

J. R. Taylor. *Introduction to Error Analysis: The Study of Uncertainties in Physical Measurements*. University Science Books, 1997.

P. K. Taylor and M. J. Yelland. The Dependence of Sea Surface Roughness on the Height and Steepness of the Waves. *Journal of Physical Oceanography*, 31(2):572–590, 2001.

M. B. van der Meulen. Influence of nonlinear irregular wave modeling on the dynamic response of an offshore wind turbine. Master's thesis, Delft University of Technology, 2012.

P. A. van Dorp. Large-eddy simulation of wind farms in clear and cloud-topped boundary layers. Master's thesis, Delft University of Technology, 2016.

E. D. van Laarhoven. Solar radiation in large-eddy simulations coupled to a general circulation model. Master's thesis, Delft University of Technology, 2019.

C. R. van Laerhoven. High-resolution atmospheric modelling and the effects on the prediction of wave characteristics. Master's thesis, Delft University of Technology, 2016.

D. K. Wilson. An alternative function for the wind and temperature gradients in unstable surface layers. *Boundary-Layer Meteorology*, 2001.

WMO. *Guide to Meteorological Instruments and Methods of Observation*. WMO, 2008.

J. Wu. Froude Number Scaling of Wind-Stress Coefficients. *Journal of the Atmospheric Sciences*, 1969.

J. Wu. Wind-stress coefficients over sea surface near neutral conditions – a revisit. *Journal of Physical Oceanography*, pages 727–740, 1980.

J. Wu. Wind-stress coefficients over sea surface from breeze to hurricane. *Journal of Geophysical Research*, 1982.